Imaging of Surface Vibrations Using Heterodyne Interferometry

Kimmo Kokkonen

Imaging of Surface Vibrations Using Heterodyne Interferometry

Kimmo Kokkonen

A doctoral dissertation completed for the degree of Doctor of Science (Technology) to be defended, with the permission of the Aalto University School of Science, at a public examination held at the lecture hall AS1 of the TUAS building (Otaniementie 17, Espoo, Finland), on 22 August 2014 at 12.

Aalto University
School of Science
Department of Applied Physics

Supervising professor
Prof. Matti Kaivola

Thesis advisor
Prof. Matti Kaivola

Preliminary examiners
Prof. Edward Haeggström
University of Helsinki, Finland
Prof. Astrid Aksnes
Norwegian University of Science and Technology, Norway

Opponents
Dr. Robert Aigner
Triquint Semiconductor, United States

NORDIC ECOLABEL

441   697
Printed matter

A'' Aalto University

Abstract

Aalto University, P.O. Box 11000, FI-00076 Aalto www.aalto.fi

Author
Kimmo Kokkonen

Name of the doctoral dissertation
Imaging of Surface Vibrations Using Heterodyne Interferometry

Publisher School of Science

Unit Department of Applied Physics

Series Aalto University publication series DOCTORAL DISSERTATIONS 112/2014

Field of research Applied Physics

Manuscript submitted 15 October 2013   **Date of the defence** 22 August 2014

Permission to publish granted (date) 7 January 2014   **Language** English

☐ **Monograph**   ☒ **Article dissertation (summary + original articles)**

Abstract

   The research summarized in this dissertation focuses on the development of a heterodyne scanning laser interferometer and of data-analysis techniques for the characterization and analysis of the surface vibration fields in microacoustic devices and test structures.

The heterodyne laser interferometer enables a phase-sensitive, absolute-amplitude detection of the out-of-plane component of a surface vibration field, with a minimum detectable amplitude of less than a picometer, while the lateral resolution is better than 1 micrometer. The instrument features a flat frequency response up to 6 GHz.

The phase-sensitive absolute-amplitude data enables the visualization of the actual wave behavior in electromechanical components and test structures, but more importantly, it is the basis for further analysis. The research instrument is applied to the study of electroacoustic devices based on surface acoustic wave (SAW) and bulk acoustic wave (BAW) technologies. Two novel SAW devices are studied in detail: a phononic crystal (PnC) structure and a scattering structure resulting in a random wave field. PnCs are acoustic metamaterials that can provide engineered material properties. The laser interferometric measurements were amongst the first to directly characterize the wave interaction with the PnC. SAW slowness curves of an anisotropic substrate material are extracted by measuring and analyzing the scattered random wave field. Data analysis methods are developed further in the context of BAW research by experimentally addressing two important aspects of device design: the correct operation of the acoustic reflector used to confine the energy in the resonator, and investigation of the role of the dispersion and standing wave resonances to the spurious responses often observed in high-Q resonators. Fourier transform techniques are used for selective visualization of wave fields and for the extraction of the dispersion characteristics of the plate-waves. The dispersion data are then further used to analyze the transfer characteristics of an acoustic reflector and to study the properties of lateral eigenresonances and the lateral energy confinement in detail.

The research described in this thesis provides a detailed characterization of the operation of SAW and BAW devices and effects within, highlighting and further developing the experimental characterization capabilities and data-analysis methods.

Tiivistelmä

Väitöskirjatyö käsittelee heterodyne-tyyppisen laserinterferometrin sekä interferometrin tuottaman datan analyysitekniikoiden kehittämistä pintavärähtelykenttien karakterisoimiseksi ja analysoimiseksi mikroakustisissa komponenteissa ja testirakenteissa.

Työssä rakennettu heterodynelaserinterferometri mahdollistaa pintavärähtelyiden vaiheherkät absoluuttiamplitudimittaukset aina 6 GHz taajuuteen asti. Laitteisto kykenee värähtelykenttien kuvantamiseen alle mikrometrin lateraaliresoluutiolla, pienimpien havaittavissa olevien värähtelyamplitudien ollessa jopa alle 1 pm. Vaihe- ja absoluuttiamplitudidata mahdollistavat värähtelykenttien visualisoinnin aaltojen todellisen käyttäytymisen ymmärtämiseksi. Mikä tärkeämpää, tämä informaatio luo pohjan edistyneille data-analyysitekniikoille.

Heterodyneinterferometriä on työssä sovellettu sähkömekaanisten, pinta- ja tilavuusaaltoihin (SAW, BAW) perustuvien komponenttien tutkimukseen. Työssä tarkastellaan kahta SAW-komponenttia: pinta-aaltokenttää akustiseen metamateriaaliin perustuvassa fononikiderakenteessa sekä sironneiden pinta-aaltojen muodostamaa satunnaista kenttää. Työssä esitetyt mittaukset olivat ensimmäisiä kokeellisia tuloksia joissa pystyttiin suoraan kuvantamaan aaltokentän käyttäytyminen fononikiteessä. Satunnaisen, sironneen, kentän mittaukset mahdollistavat pinta-aaltojen hitauskäyrän määrittämisen pietsosähköiselle anisotrooppiselle kiteelle.

Data-analyysimenetelmiä on kehitetty keskittyen kahteen, erityisesti BAW-komponenttikehityksen kannalta keskeiseen asiaan: akustisen peilin toiminnan tutkimiseen ja aaltojen dispersio-ominaisuuksien sekä lateraaliresonanssien ja niihin liittyvien ei-toivottujen sähköisten vasteiden tutkimiseen korkean hyvyysluvun resonaattoreissa. Fourier-muunnokseen pohjautuvia tekniikoita käytetään aaltokenttien selektiiviseen visualisointiin ja laattaaaltojen dispersio-ominaisuuksien selvittämiseen. Dispersiodataa hyödynnetään edelleen akustisen peilin vasteen selvittämiseksi, lateraalisten ominaisresonanssien sekä resonaattorin energian lateraalisen rajoittamisen yksityiskohtaiseen analyysiin.

Väitöskirjan tutkimustyö tarjoaa yksityiskohtaisen kuvauksen SAW- ja BAW-laitteiden toiminnasta ja niissä esiintyvistä ilmiöistä, tuoden erityisesti esiin kokeellisen tutkimuksen tarjoamia mahdollisuuksia ja edelleen kehittäen data-analyysimenetelmiä.

Preface

The research work summarized in this dissertation begun in the Materials Physics Laboratory at Helsinki University of Technology, and following the untimely death of Professor Martti Salomaa, was continued under the supervision of Professor Matti Kaivola in what became Department of Applied Physics, Aalto University School of Science. I am grateful for both Professors for their guidance and for the opportunity to work in this fascinating field of research.

The work was carried out in national and international collaboration, most notably with VTT Technical Research Centre of Finland, and with Femto-ST, France, respectively. I have enjoyed a long-time collaboration with Tuomas Pensala, who has contributed significantly to several publications included in this thesis. I also wish to thank numerous other people from VTT, many of which are not co-authors in the publications included in this thesis, but with whom I have had great discussions and who have expressed their interest in this work. My French collaborators, Vincent Laude and Sarah Benchabane, deserve a special thank you for the very enjoyable and productive collaboration.

A special thank you to all my friends who have been my support throughout these years. Jukka Paajanen is especially acknowledged for his expert help in getting a stubborn piece of code to work.

I had the privilege to work for years with the wonderful people of Materials Physics Laboratory and particularly of the SAW group. I will always remember the enjoyable atmosphere and our lively discussions. I would like to thank the colleagues for the scientific discussions, encouragement and support as well as for the good company on many enjoyable

To my parents, to my wife and to my son.

July 10, 2014,

Kimmo Kokkonen

Contents

iv

List of Publications

This thesis consists of an overview and of the following publications which are referred to in the text by their Roman numerals.

I K. Kokkonen, and M. Kaivola. Scanning heterodyne laser interferometer for phase-sensitive absolute-amplitude measurements of surface vibrations. *Applied Physics Letters*, 92, 063502, 2008.

II K. Kokkonen, M. Kaivola, S. Benchabane, A. Khelif, and V. Laude. Scattering of surface acoustic waves by a phononic crystal revealed by heterodyne interferometry. *Applied Physics Letters*, 91, 083517, 2007.

III V. Laude, K. Kokkonen, S. Benchabane, and M. Kaivola. Material anisotropy unveiled by random scattering of surface acoustic waves. *Applied Physics Letters*, 98, 063506, 2011.

IV K. Kokkonen, T. Pensala, and M. Kaivola. Dispersion and Mirror Transmission Characteristics of Bulk Acoustic Wave Resonator. *IEEE Transactions on Ultrasonics, Ferroelectrics and Frequency Control*, 58, 215 – 225, 2011.

V K. Kokkonen, T. Pensala, J. Meltaus, and M. Kaivola. Extraction of lateral eigenmode properties in thin film bulk acoustic wave resonator from interferometric measurements. *Applied Physics Letters*, 96, 173502, 2010.

VI K. Kokkonen, J. Meltaus, T. Pensala, and M. Kaivola. Characterization of energy trapping in a bulk acoustic wave resonator. *Applied Physics Letters*, 97, 233507, 2010.

VII K. Kokkonen, J. Meltaus, T. Pensala, and M. Kaivola. Measurement of Evanescent Wave Properties of a Bulk Acoustic Wave Resonator. *IEEE Transactions on Ultrasonics, Ferroelectrics and Frequency Control*, 59, 557 – 559, 2012.

Author's contribution

The Author has contributed significantly to the planning, implementation, analysis, interpretation and reporting at all stages of the research reported in this thesis. The Author has solely designed, constructed and characterized the research instrumentation reported in Publication I and used it to conduct the research reported in the other Publications appended in this thesis. All of the experimental work, except the fabrication of the samples and their wafer level electrical characterization has been carried out by the Author. The Author has developed the new data analysis concepts regarding the advanced and further use of the dispersion diagrams, presented in Publications IV, V, VI, and VII. The Author has been primarily responsible for writing the Publications I,II, and IV-VII, and responsible for the experimental part and data analysis of Publication III. The Author has also presented results reported in this thesis as an invited speak at IEEE International Ultrasonics Symposium 2009 and at several other international conferences.

List of abbreviations

The following abbreviations are used in the overview:

AFM	Atomic force microscopy
AOM	Acousto-optical modulator
BAW	Bulk acoustic wave
BG	Band gap
BW	Bandwidth
COM	Coupling of modes
FEM	Finite-element method
FBAR	Film bulk acoustic resonator
FT	Fourier transform
FWHM	Full width at half maximum
IDT	Interdigital transducer
mBvD	Modified Butterworth van Dyke
PBS	Polarizing beam splitter
PD	Photodetector
PnC	Phononic crystal
QP	Quadrature point
RF	Radio frequency
SAW	Surface acoustic wave
SEM	Scanning electron microscopy
SMR	Solidly mounted resonator
SNR	Signal-to-noise ratio
TE	Thickness extensional
TS	Thickness shear

x

1. Introduction

The ongoing development of mobile electronics devices and telecommunications applications has created a demand for increasingly better electrical components. High-performance radio frequency (RF) and microwave filters are central for the wireless transmission and reception of signals in mobile communication devices. To meet the demanding specifications, the filtering of electrical signals is realized by electroacoustic means, where the electrical signal is transformed into mechanical domain and back, for example via the piezoelectric effect. Currently mobile communications devices use filters based on both surface acoustic wave (SAW) and bulk acoustic wave (BAW) technologies. At the same time with requirements for better performance, the operation frequencies are shifting further up in the frequency. Therefore, the performance limits of SAW and BAW technologies are constantly pushed further, in terms of low loss, improved power handling capability, smaller size, better system integration, suppression of non-linear effects and functionality.

Acoustic waves are perturbations of an elastic medium that cause displacements of small volumes of matter from their equilibrium position. The waves propagate in the medium with a characteristic velocity and can travel either with their energy localized near the surface (SAWs) or inside the bulk of the medium (BAWs). Elastic waves can also have displacements in the direction of their propagation (longitudinal waves), or in the directions perpendicular to the propagation (shear or transverse waves), or be a combination of the two as is typical for propagation in anisotropic solids. Lord Rayleigh discovered a solution to the wave equation describing waves with their energy localized to a surface in 1885 [1], predicting the existence of SAWs. Jacques and Pierre Curie had discovered the piezoelectric effect in 1880 [2], and the subsequent research on piezoelectric materials, in which a deformation creates an electric field in

the material, and where an electric field results in a material deformation, enabled generation and reception of acoustic waves (SAWs and BAWs) for practical use. A structure to efficiently transduce an RF electrical signal into SAW and back was reported by White and Voltmer in 1965 [3]. This structure, an interdigital transducer (IDT), together with piezoelectric materials, enabled the industrial utilization of acoustic waves in signal processing and filtering applications.

The performance of electroacoustic signal processing and filtering devices is ultimately determined by their electrical response. Therefore, they are typically characterized via electrical measurements, in test structures and in actual device configurations. Research and development of electroacoustic devices has, indeed, benefitted substantially from the advances in electric measurement technology, such as from modern vector network analyzers. Operation of an electroacoustic device is, however, based on the (electro)mechanical response, and therefore even a thorough electrical characterization provides only indirect information of the wave motion and of the underlying device physics. In the case of a mismatch between a designed and an actual response, the electrical characterization often leaves open questions on the details of the mechanical behavior. For a better understanding of wave motion in anisotropic materials and in complex micro- and nanostructures, direct information of the vibration field is needed. These data provide crucial feedback for further development of theoretical understanding of wave phenomena as well as vital information for improved device designs.

To address the need for the characterization of the surface vibrations, various methods, both contact and non-contact, have been developed. Optical probing techniques enable a direct, non-contact measurement of the vibration fields on the sample. Especially with complex structures, such as multilayered devices or phononic crystals, optical probing can contribute significantly to the understanding of the device physics, providing feedback for the development of device modeling. For the best results, optical probing should be combined with electrical measurements to acquire the most complete picture of the device behavior.

The research summarized in this thesis focuses on the development of a heterodyne scanning laser interferometer and of data-analysis techniques, which are applied to experimentally characterize surface vibra-

tion fields in microacoustic devices. The measurement principle, the design and performance of the heterodyne laser interferometer are discussed first. This is followed by application of the research instrument to study SAW and BAW devices and effects within, highlighting and further developing the experimental characterization capabilities and data-analysis methods.

2. Optical characterization of surface vibrations

After the invention of the laser in the 1960s [4], optical probing of surface vibrations has seen wide-spread use as a research tool to deepen the understanding of wave physics in various materials, in combinations of materials and in different device configurations. The three main operation principles of the early instruments were based on the diffraction grating technique, the knife-edge technique and on various forms of interferometry. The diffraction grating and knife-edge techniques are well suited to measurement of SAWs, since they depend on the formation of surface relief grating and on surface tilt, respectively. The diffraction grating technique was a popular approach in the 1970s [5–7], but has not been widely used recently. The knife-edge technique has also been successfully applied by many authors to investigate wave propagation, for example to separate propagating and standing wave contributions, to measure SAW velocities, attenuation, beam steering and diffraction [8–16]. For a recent implementation of this technique to phase-sensitive optical probing of SAW vibration fields and data-analysis, see Refs. [17–20].

When the surface features spatially smooth wave fields, such as in some BAW applications, optical interferometry has advantages over the above-mentioned methods, since it enables a direct measurement of the surface displacement. Interferometers have gained popularity as the optical detection method of choice and several setups have been published [21–33]. A more thorough compilation of references related to optical probing of SAWs and the extraction of various propagation properties can be found in Ref. [34].

In addition to the measurement techniques falling into these main categories, research instruments with their detection based on the variation of some other optical quantity caused by acoustic wave propagation in the material have been reported. These instruments may operate in reflection

mode, such as typical laser interferometers, or, e.g., by light transmission through the material [35,36]. One example of the latter is an optical probe in which the polarization of a laser beam traveling through the bulk of the material is modulated by elastic waves within the medium [37–39]. There exists also a broad class of instruments utilizing laser speckle phenomena for displacement and vibration measurement. For a recent application of speckle-based techniques, see Ref. [40]. Holographic approaches have also been used in vibration measurements since the late 1960s, see, e.g., Refs. [29, 41–43].

There have been a number of attempts to characterize vibrations with various other means also. One example is the use of atomic force microscopy (AFM) to characterize surface vibrations [44–47]. It cannot be considered as a truly non-contact method, as it can significantly influence the sample under study [48], although techniques have been developed to minimize the effect [49]. In fact, many of the available microscopy techniques, such as scanning electron microscopy (SEM) [50], have been adapted to study also surface vibrations. In addition to various scanning probe microscopy techniques, there have been attempts to visualize surface vibrations also with several other more exotic techniques, some of which are not non-destructive or non-contact [51–53].

In addition to the laser interferometric techniques with frequency domain detection discussed in this thesis, optical laser-based time-domain pump-probe techniques have been used in the study of acoustic wave propagation, thin-film materials properties and surface vibrations [54]. These picosecond ultrasonic pump-probe techniques utilize excitation of elastic waves by an optical pump-pulse and the subsequent detection of the waves by a time-delayed optical probe beam [55, 56]. The technique is well-suited for characterizing acoustic properties of bulk [57, 58], as well as of thin-film samples [59], such as those used in acoustic mirrors of solidly mounted BAW devices. Instead of a single-point measurement, the sample may also be scanned to obtain two-dimensional images of wave propagation [60, 61]. The technique has recently also been applied to study wave interaction with phononic crystal samples [62–65].

Because the history of optical probing of surface vibrations dates back to the 1960s and beyond, there exist several excellent review articles [22, 66–68], books [69–73] and book chapters [74–78] on the various optical detection methods.

2.1 Scanning laser interferometry in frequency domain

In physical acoustics, it is important to be able to detect and characterize small surface vibrations. Vibration amplitudes vary greatly depending on the type of device and application, but in the case of SAW and BAW research for ultrasonic applications ($f > \mathrm{MHz}$), the typical maximum amplitudes are of the order of a few nanometers or less. Therefore, in order to ensure a good signal-to-noise ratio (SNR) of the measurement and to be able to study weak effects, the minimum detectable vibration amplitude should be of the order of 1 picometer or less, which is roughly 1/100 of the size of an atom. Furthermore, as operating frequencies range from MHz to several GHz, the detection method should have a flat frequency response to allow quantitative vibration analysis. In addition, since the devices often are sensitive to perturbations from the surroundings and have high Q-values, a non-contact method is necessary.

Laser interferometry offers a non-contact optical method, which can be used to detect such vibrations. In the conceptually simple case of a homodyne Michelson interferometer (see Fig. 2.1), the interferometer consists of a measurement arm and a reference arm. The sample with a vibrating surface is placed in the measurement arm. The surface vibration leads to a variation of the optical path length of the measurement arm, resulting in an optical phase modulation with respect to the reference beam. The laser interferometer converts the optical phase difference between the two laser beams into a variation of light intensity via the interference of the beams. The resulting intensity signal can then be measured with a photodetector. In this way, the length reference for the measurement is derived from the well defined laser transition, which in the case of red HeNe laser is $\lambda = 632.8$ nm.

In the following, we concentrate on scanning laser interferometry with sinusoidal electrical excitation of the vibrations in the sample and their detection in the frequency domain. This concept has proved very successful in SAW and BAW device research, where the samples are excited electrically and the resulting wave fields within the samples can be measured with an interferometer. As the excitation frequency can be precisely controlled, the frequency domain operation allows for a detailed study of
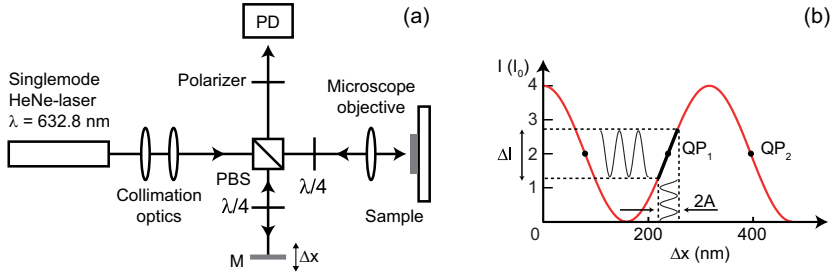
Figure 2.1. Schematic presentation of a Michelson interferometer and the detected signal. (a) Optical setup of a Michelson laser interferometer. Linearly polarized laser beam is collimated and split into the two arms of the interferometer by a polarizing beam splitter (PBS). The reference beam travels through a quarter-wave plate ($\lambda/4$) to a mirror and back. The measurement beam travels also through a $\lambda/4$-plate and is focused, by a microscope objective, onto a spot on the sample surface, from which it is reflected back. The two beams are recombined at the PBS and travel through a polarizer to a photodetector (PD). (b) Illustration of the interferometer signal as a function of reference mirror displacement (Δx). The black dots mark the quadrature points (QPs), offering maximum sensitivity and best linearity. In these operation points, the smallest surface vibration amplitude A results in the largest change in the detected light intensity ΔI.

the mechanical resonances and vibration modes arising in the structures. Furthermore, by limiting the detection bandwidth, the noise floor of the measurement is lowered and SNR enhanced, allowing for the detection of small vibration amplitudes, even below 1 pm.

2.1.1 Homodyne detection

The homodyne interferometer setups used in physical acoustics research are typically based on either Michelson or Mach-Zender interferometer configurations. An example of a Michelson-type homodyne interferometer is depicted in Fig. 2.1(a) and a schematic presentation of the interferometer signal due to a change in the optical path length is presented in Fig. 2.1(b). Here the signal is considered to be devoid of noise or of any other unidealities.

Consider a one-dimensional case, where two coherent monochromatic waves of equal optical frequencies and in the same polarization state are superimposed. The constituent waves have intensities I_1 and I_2 and optical phases θ_1 and θ_2, respectively. Denoting the phase difference $\varphi = \theta_2 - \theta_1$, the basic equation for two-beam interference is

$$I(\varphi) = I_1 + I_2 + 2\sqrt{I_1 I_2} \, \cos(\varphi). \tag{2.1}$$

The last term of Eq. (2.1), the interference term, may be either positive or negative, corresponding to a constructive or destructive interference of

the two waves. In the special case of interference between two waves with equal intensities ($I_1 = I_2 = I_0$), the resulting intensity $I(\varphi)$ varies between 0 and $4I_0$, see Fig. 2.1(b). The optical phase difference φ carries the information of the varying optical path length of the interferometer and, hence, ultimately that of the surface vibration to be probed. Therefore, the interference of the waves serves to convert a small optical path length difference between the two beams into an intensity variation that can be measured with a photodetector.

A sinusoidal surface displacement, $A \sin(2\pi f_{\mathrm{vib}} t + \phi_{\mathrm{vib}})$, where A is the amplitude and ϕ_{vib} is the phase of the surface vibration under study, results in a time-dependent variation of the optical phase difference,

$$\varphi(t) = \varphi_0 + \frac{4\pi A}{\lambda} \sin(2\pi f_{\mathrm{vib}} t + \phi_{\mathrm{vib}}), \tag{2.2}$$

where f_{vib} is the frequency at which the sample is electrically excited (with the assumption of a linear mechanical response), λ is the wavelength of the laser light and φ_0 is a slowly varying phase term (compared to f_{vib}) that represents the optical phase difference between the two beams due to changes in ambient conditions. Substituting Eq. (2.2) into Eq. (2.1), and in the limit of small vibrations (for linear detection, typically $A < 10$ nm), the homodyne detection equation can be approximated as [34, 79–81]

$$\begin{aligned} I(t, \varphi_0) = I_1 + I_2 + 2\sqrt{I_1 I_2} \\ \times \left[\cos(\varphi_0) + \frac{4\pi A}{\lambda} \sin(2\pi f_{\mathrm{vib}} t + \phi_{\mathrm{vib}}) \sin(\varphi_0) \right]. \end{aligned} \tag{2.3}$$

From Eq. (2.3), it is evident that in homodyne detection the optical phase difference φ_0 between the two beams has to be controlled in order to detect the contribution from the surface vibration. To obtain both the highest sensitivity and the best linearity in the detection of small vibrations, the interferometer is operated at the so-called quadrature point (QP), where $\sin(\varphi_0) = 1$, see Fig. 2.1(b). Knuuttila et al. [27] solved the problem of optical phase control by mechanically scanning the path length in one of the arms using a piezo-controlled reference mirror, while recording the interference signal with a spectrum analyzer tuned to the frequency of the vibration. In this scheme, an active path-length stabilization is not required for the acquisition of the relative amplitude data of the vibration. Since the method uses a spectrum analyzer for the detection and does not discern between the up-slope and down-slope quadrature points (QP_1 and QP_2 in Fig. 2.1(b)), phase information of the surface vibration is

lost. The technique has been further refined such that during the mirror-sweep, also the (low frequency) interference signal is recorded, which allows phase-sensitive measurements of the surface vibration by using a vector network analyzer for the sample excitation and signal detection. Furthermore, the low frequency signal carries also information of the quality of the interference, and hence, with a calibration measurement, also absolute amplitude data can be obtained [82].

The optical path length control can also be realized by actively stabilizing the interferometer into a QP (see, e.g., Refs. [28, 83]). The role of the stabilization is to compensate for any slow drifts between the optical path lengths of the two interferometer arms, typically caused by air flows, thermal expansion, or simply by differences in the heights of the features on the sample surface. The stabilization counteracts this change, for example, by slightly displacing the reference mirror, in order to ensure operation at the chosen QP. Stabilized setups enable phase sensitive detection of the vibrations, for example, via sample excitation and measurement of the photodetector signal with a vector network analyzer. Acquisition of absolute amplitude data requires an additional measurement to quantify the system gain and to compensate for gain drift caused by differences in the optical reflectivity of the sample surface, the drift in the quality of interference, etc.

3. Scanning heterodyne laser interferometer

The scanning heterodyne laser interferometer developed for microacoustics research and used in this thesis has the optical setup of a modified Mach-Zehnder interferometer, see Fig. 3.1. A linearly polarized and collimated beam from a single-mode HeNe laser (Spectra-Physics model 117A) is split in two in an acousto-optical modulator (IntraAction model AOM-405A1) (AOM), where the reference beam (I in Fig. 3.1) acquires an optical frequency shift with respect to the zeroth-order beam (0). The zeroth-order beam is the probe beam that is focused with a microscope objective (Nikon 50x/0.55 ELWD) to a ~ 820 nm sized spot (full width at half maximum, FWHM) on the sample surface. A $\lambda/4$ plate rotates the polarization plane of the probe beam to facilitate correct beam steering at the polarizing beam splitter (PBS), where the two, now orthogonally polarized, beams are combined. The beams then propagate through a linear polarizer to a fast (0 - 12 GHz) photodetector, which features a flat frequency response (better than ± 1 dB up to 6 GHz) (New Focus model 1554-A)(PD). The sample is raster scanned under the focused laser beam by computer-controlled motor stages (Newport M-MFN25cc) providing a 25 mm range of motion along each of the three axes, capable of a smallest incremental step size of 55 nm.

Consider the interference of two laser beams with intensities I_1 and I_2 originating from the same laser source. If one of the beams is shifted in frequency from the original optical frequency f to $f + f_\mathrm{m}$ ($f_\mathrm{m} \ll f$), the interference signal averaged over the optical cycle is

$$I(t) = I_1 + I_2 + 2\sqrt{I_1 I_2} \cos\left(2\pi f_\mathrm{m} t + \varphi(t)\right), \qquad (3.1)$$

where $\varphi(t)$ is the optical phase difference between the beams. When one of the beams is reflected back from a sinusoidally vibrating sample surface,

11

the phase difference can be written as

$$\varphi(t) = \varphi_0 - \frac{4\pi}{\lambda} A \cos\left(2\pi f_{\mathrm{vib}} t + \phi_{\mathrm{vib}}\right), \qquad (3.2)$$

where A is the amplitude of the normal component of the surface vibration, λ is the wavelength of the laser light, and f_{vib} and ϕ_{vib} are the frequency and phase of the vibration, respectively. The term φ_0 is a slowly varying phase term (compared to f_{vib}) that represents any arbitrary optical phase variations between the two arms of the interferometer due to, e.g., variations in the ambient conditions. When the surface-vibration amplitude (A) is small compared to λ, the interference term of Eq. (3.1) may be expanded as [23]

$$\begin{aligned} I_{12}(t) = \ 2\sqrt{I_1 I_2}\Big[&\cos\left(2\pi f_{\mathrm{m}} t + \varphi_0\right) + \\ &\frac{2\pi A}{\lambda}\Big\{ \cos\left(2\pi \left(f_{\mathrm{m}} + f_{\mathrm{vib}}\right) t + \phi_{\mathrm{vib}} + \varphi_0\right) \\ &- \cos\left(2\pi \left(f_{\mathrm{m}} - f_{\mathrm{vib}}\right) t - \phi_{\mathrm{vib}} + \varphi_0\right)\Big\}\Big]. \end{aligned} \qquad (3.3)$$

The error in the calculated amplitudes due to this approximation is less than 1 %, when $A \le 10$ nm and $\lambda = 632.8$ nm.

When observed in the frequency domain, the signal spectrum consists of a modulation peak (at f_{m}) and two satellite peaks (at $f_{\mathrm{m}} \pm f_{\mathrm{vib}}$). When measuring actual samples, only the modulation peak and the upper ($f_{\mathrm{m}} + f_{\mathrm{vib}}$) satellite peak (hereafter called the signal peak) are detected (see Fig. 3.1(b)). The modulation and signal peaks (at two frequencies) are detected simultaneously and the absolute amplitude of the surface vibration can be acquired from their amplitude ratio. Also, by comparing the phases of the two signals, the phase of the surface vibration is acquired, and any slow variations in the optical path lengths cancel out. The ability to measure the absolute amplitude of the surface vibration provides immunity to effects such as variations in the local optical surface reflectivity of the sample. Furthermore, the heterodyne detection diminishes potential problems caused by radio frequency (RF) leakage as there is a frequency offset between the detected frequency ($f_{\mathrm{m}} + f_{\mathrm{vib}}$) and the frequency at which the sample is driven (f_{vib}).
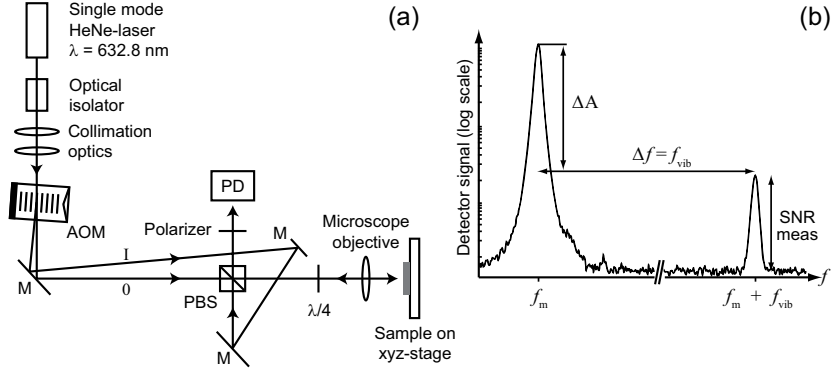
Figure 3.1. (a) Optical setup of the scanning heterodyne laser interferometer. (b) Schematic, frequency-domain presentation of the heterodyne signal detected from the photodetector. The acousto-optical modulator (AOM) splits the laser beam into two, a measurement beam (0) and a reference beam (I). The reference beam acquires an optical frequency shift in the AOM, and the frequency difference between the two beams (f_m) will result in the modulation peak in the detected frequency spectrum. The signal detected due to the surface vibration (at f_{vib}) is also frequency shifted (to $f_m \pm f_{vib}$), hence also diminishing the possibility of RF-leakage (from the sample to the detection). The dynamic range of the setup is defined by the ratio of the amplitude of the modulation peak compared to the noise floor, defining also the minimum detectable amplitude. The signal to noise ratio of the measurement (SNR) corresponds to the ratio between the maximum vibration amplitude and the noise floor.

3.1 Performance of the setup

The principal performance attributes of a scanning laser interferometer are the minimum detectable amplitude, immunity to variations in the optical reflectivity of the sample surface, scanning speed and lateral resolution. The most important of these parameters is, perhaps, the minimum detectable amplitude, since it ultimately sets the limit on how small signals and how weak effects can be studied with the setup. Furthermore, in frequency domain detection, where a frequency sweep is utilized, the minimum detectable amplitude and the speed of the frequency sweep are interconnected through the bandwidth (BW) of the detection electronics. Selecting a larger detection BW allows for faster frequency sweeps, with a tradeoff between the measurement noise level and the sweep speed. A sensitive setup allows one to sacrifice some signal for speed, while still maintaining an acceptable level of minimum detectable amplitude.

The achievable lateral resolution is ultimately limited by diffraction to the order of the wave length of the laser light used. For the majority of applications in SAW and BAW research, the lateral resolution of $\sim 0.5~\mu$m is sufficient. Achieving significantly better lateral resolution with laser interferometers is challenging.

13

3.1.1 Minimum detectable amplitude

With the setup reported in Publication I, and a detection bandwidth of 30 Hz, the smallest detectable surface vibration is ~ 1 pm, as measured from an actual sample. This corresponds to a measurement sensitivity of $\sim 2 \times 10^{-4}$ nm/$\sqrt{\text{Hz}}$. The theoretical detection limit for a heterodyne interferometer (perfect interference, shot noise limited detection) is given by [22, 84]

$$A_{\min} = \sqrt{\frac{2eBW}{\alpha P_o}} \frac{\lambda}{\pi},$$ (3.4)

where e is the elementary charge, BW the detection bandwidth, P_o the total optical power, α the responsivity (A/W) of the photodetector and λ the wavelength of the laser. Using a value of 0.5 mW for the optical power, 0.2 A/W for the responsivity and 632.8 nm for the laser wavelength results in a theoretical detection limit of $\sim 1 \times 10^{-5}$ nm/$\sqrt{\text{Hz}}$, which with 30 Hz detection bandwidth corresponds to $A_{\min} \sim 0.05$ pm. The difference between the obtained and theoretical sensitivity is mainly due to the limited optical power available at the photodetector, which results in a reduction of the available dynamic range. The measurement speed of the system depends on the chosen BW. A detection bandwidth of 30 Hz results in a scanning speed of $\sim 94\,000$ spatial scanning points per hour (pnt/h), which can be increased by choosing a larger BW at the cost of an increase in the noise level.

By increasing the available laser power incident on the photodetector, the system was improved such that the smallest detectable surface vibration amplitude is now ~ 0.3 pm, as measured from an actual sample (measurement results reported in Publication IV), with a detection bandwidth of 100 Hz. For these measurements, the scanning speed was $\sim 270\,000$ pnt/h.

3.1.2 Lateral resolution

In a scanning laser interferometer, the laser beam is focused onto the sample surface. The sample is then raster scanned under the laser spot with a chosen lateral scan step to produce an image of the surface vibration field. The laser spotsize on the sample surface therefore determines the lateral resolution obtainable with a given setup.

Diffraction ultimately limits the minimum achievable spotsize on the sample surface. Trying to get a spot as small as possible might not be

feasible, since as the spot size on the sample gets smaller, the depth of focus of the laser beam correspondingly diminishes. This results in an increasingly stringent tolerance on the distance from the focusing lens to the sample surface. In our setup, there is no active focusing adjustment such that the objective-to-sample distance would be actively controlled. Instead, the sample is aligned such that the sample surface is normal to the incident laser beam, and hence, only the sample topography will chance the distance to the lens during scanning. Therefore, it is desirable that the interferometer would tolerate height differences (changes in focus) of the order of ± 1 μm. This is achieved with a spot size of a gaussian laser beam of ~ 820 nm (measured as FWHM on the sample surface), offering a lateral resolution better than 1 μm. The obtained lateral resolution is sufficient for all typical devices for microacoustic applications (e.g., SAW and BAW), with operating frequencies upto several GHz.

3.1.3 Immunity to variations in optical reflectivity

In typical microacoustic samples (SAW and BAW), there are areas of different optical reflectivity on the sample surface. For example, in the case of a typical SAW device, there is the crystalline substrate, such as $LiNbO_3$, with a very low reflectivity, and metalized regions on top of it, with a very high reflectivity. The changes in the optical reflectivity change the relative intensities of the interfering laser beams. In the case of a simple Michelson interferometer, this causes a change in the sensitivity, leading into discontinuities in the measured amplitude on the sample across such a boundary (consider, for example, a transition from crystal to metal). In general, any change in the sample surface (surface roughness, different height leading to change in focus, etc.) or a drift in the optical setup that leads to a change in the quality of the interference will result in a discontinuity in the detected amplitude values.

In the heterodyne interferometer (Publication I), the quality of the interference is monitored via the modulation signal (for an illustration, see Fig. 3.1(b)), and the ability to measure the absolute amplitude of the surface vibration provides immunity against effects due to variations of the optical surface reflectivity on the sample. An example of actual measured amplitude data with SAWs traveling over a crystal-to-metal transition is provided in Fig. 3.2. The example data serve to show that the detected absolute-amplitude field is continuous despite the large difference in the optical reflectivities between the crystalline and metalized regions. This

highlights the correct operation of the heterodyne setup. The obvious limitation is a case in which the SNR of the measurement is enough to detect the weak vibration on the metal surface, but the low optical reflectivity of the crystal surface leads to reduced SNR, and does not allow the detection of such low amplitudes anymore. In other words, the differences in the optical surface reflectivity and quality of the interference can be seen in the heterodyne interferometer data as changes in the measurement noise level in areas without vibration amplitude.
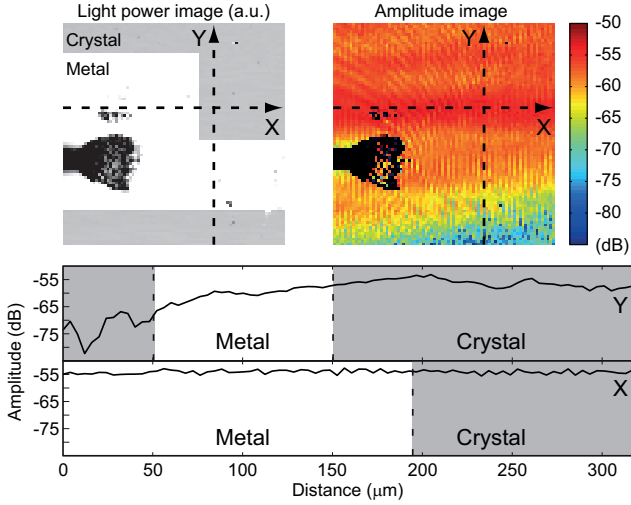

Figure 3.2. Demonstration of heterodyne absolute-amplitude detection, where a discontinuity in the optical surface reflectivity of the sample does not influence the detected surface vibration amplitude values. Light power image, on the left, depicts a close-up view of the sample, showing both an aluminized bond pad and a crystal surface as well as a bondwire providing electrical connection to the sample. The corresponding measured vibration amplitude field is continuous over the discontinuities in the optical surface reflectivity. Line profiles (in X and Y directions, marked with dashed lines in the light power and amplitude images) do not show any amplitude discontinuities at the transition points (marked with dashed vertical lines).

3.2 Data analysis based on Fourier methods

Accurate, good quality data acquired with a carefully built heterodyne interferometer can be used not only to visually inspect and interpret the acoustic vibration fields in a sample, but also as a basis for further data analysis. Analysis methods based on Fourier transform (FT) techniques have proven successful and are widely utilized, especially in BAW research. The phase sensitive absolute-amplitude data, representing the surface vibration fields in the sample, are in general superpositions of sev-

eral wave modes that exist simultaneously at a given excitation frequency. The FT provides a modal decomposition of the measured resultant wave field, and allows to, for example, determine the lateral (parallel to the sample surface) component of the wave vector $k_{||} = 2\pi/\lambda_{||}$, and hence, to separate SAWs propagating into different directions in the measurement area, to analyze reflections and to determine wave slowness ($\mathbf{k}_{||} = 2\pi f \mathbf{v}_{||}^{-1}$) experimentally, see Fig. 3.3 for a schematic presentation.

In the following, two applications of FT techniques are discussed in more detail. Measuring wave fields at several excitation frequencies allows experimental determination of the plate-wave dispersion properties, an important issue in BAW research and device development. Selective visualization of wave fields can be achieved by filtering selected spatial frequencies in the Fourier domain and applying an inverse transformation. This technique allows to visualize the wave fields corresponding to the selected wave mode(s). In some cases, the use of Fourier filtering allows to extend the dynamic range of the measurement by suppressing noise, and can therefore be used in the characterization of extremely weak signals and effects. In the research reported in this thesis, especially the BAW dispersion measurement and data-analysis has been pushed beyond the current state of the art, thanks to the high-quality interferometer data and advanced data analysis.
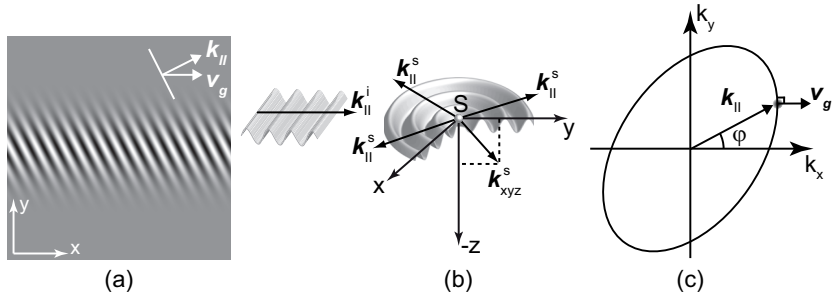

(a) (b) (c)

Figure 3.3. Schematic presentation of wave propagation in an anisotropic medium. (a) An example of instantaneous surface displacement field for SAW beam propagation on an anisotropic medium featuring a power flow angle. (b) General case of SAW scattering. An incident plane-wave SAW with wave vector $\mathbf{k}_{||}^i$ is scattered from the scatterer S into all directions, resulting in scattered SAWs with wave-vectors parallel to the crystal surface $\mathbf{k}_{||}^s$ and waves scattered into the bulk with $\mathbf{k}_{xyz}^s$ propagating to all directions in the volume. (c) Schematic presentation of the slowness curve for the anisotropic medium in (a), with the lateral wave vector $\mathbf{k}_{||}$ and group velocity vector $\mathbf{v_g}$ that indicates the direction of power flow shown. The SAW field in (a) corresponds to a single point in the FT result, indicating the direction and magnitude of the wave vector. Scattering into all (in-plane) directions, as depicted in (b), will then reveal the slowness curve.
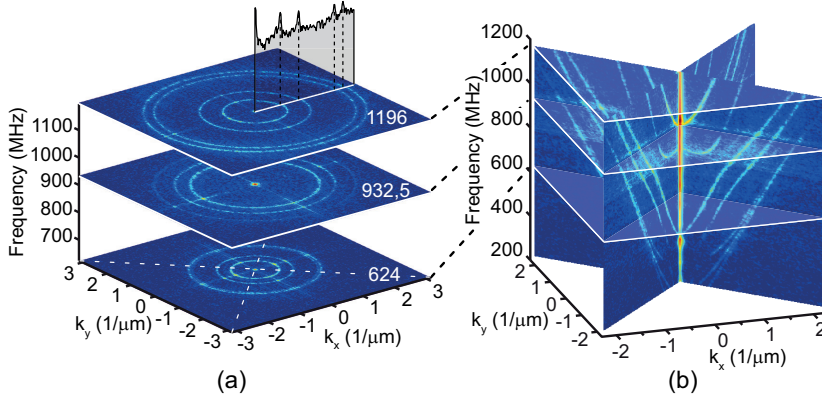
Figure 3.4. (a) Illustration of BAW FT result for a set of three frequencies, with the magnitude of the FT along $|\mathbf{k}_{x+}|$ plotted on the top (for 1196 MHz). (b) A volume visualization of general dispersion data with two slice planes (plane directions indicated with white dashed lines in (a)). The general dispersion data consist of a stack of FT results at all the measured frequencies, and contains the dispersion information for waves traveling to all directions (in the scanplane). Due to the nature of the thin-film manufacturing, usually an in-plane isotropy of the material is assumed and for visualization purposes, typically the directional information is disregarded by circularly averaging the data and the wave content is plotted as a function of frequency and magnitude of the wave vector $|\mathbf{k}_{\parallel}|$, see Fig. 3.5.

3.2.1 From wave field measurement to dispersion diagram

The FT of a measured complex-amplitude wave field is a modal decomposition of the field revealing directional information on the wave propagation. In the general case of wave propagation in anisotropic media, the magnitude of the in-plane (lateral) components of the wave-vectors for a given wave mode have an angular dependence due to the angular dependence of the phase velocity of the wave mode. Since the wave field measurement enables to quantify the lateral component of the wave vector at a given excitation frequency, the propagation direction and wavelength are acquired through the measurement. This allows one to study the dispersion properties of the waves by repeating the measurement and analysis at several frequencies.

In connection with BAW resonators, typically the sputtered piezoelectric thin film is considered to be in-plane-isotropic, and hence, the magnitude of the lateral component of the wave vector is assumed not to have any angular dependence. This leads to circles observed in the FT result, indicating wave propagation to all directions in plane, e.g., due to scattering (see Fig. 3.4 (a)). To be able to characterize not only the wave content at a single frequency, but the dispersion properties of the different wave

modes, the wave-field measurements and their Fourier analysis have to be performed at a number of frequencies. At each frequency, the wave content can be visualized in the wave-vector space (see the FTs in Fig. 3.4 (a)), and having several frequencies leads to a multidimensional data set. In general, volume visualization techniques may be applied, e.g., by defining slice-planes to show the wave content and the frequency dependence of the wave-vector in a direction of interest, Fig. 3.4 (b). On the other hand, the wave-content (2D propagation in scan-plane) at each frequency may be reduced to a single line (1D) by either taking a line profile along the direction of interest (such as x- or y-direction in the case of square resonator symmetry, see Fig. 3.5) or, if in-plane isotropy is assumed, by circularly averaging the wave content as a function of the magnitude of the in-plane wave-vector ($|\mathbf{k}_\parallel|$). Presenting the acquired data as a function of frequency yields a dispersion diagram for the lateral wave-vector component of the waves propagating in the structure. The procedure to acquire a plate-wave dispersion diagram from wave field measurements of a BAW resonator is illustrated in Fig. 3.5. Note that the wave-vector information in each frequency-slice in the dispersion diagram is proportional to the slowness, the inverse of the phase velocity, of the wave mode(s) ($\mathbf{v}_\parallel^{-1} = \mathbf{k}_\parallel / 2\pi f$), while the local slope of a mode branch in the dispersion diagram presents the group velocity ($df/d\mathbf{k}_\parallel = \mathbf{v}_{\mathbf{g}\parallel}/2\pi$) at that frequency.

In an actual finite-sized sample, the resonator geometry determines the lateral standing-wave resonances arising in the resonator structure. For example, a square resonator has separable x- and y-directional standing wave resonances and correspondingly these resonances result in bright spots in the wave-vector domain (see Fig. 3.5). Wave scattering also leads to waves traveling into all possible directions, and hence there is typically a circle in the wave-vector domain, together with the geometry related maxima (bright spots).

3.2.2 Filtering of wave field data in wave-vector domain

In addition to visualizing the wave content in the Fourier domain (wave vector space), the FT techniques also enable visualization of selected wave components by utilizing filtering in the Fourier domain and applying an inverse transform. In this method, a range of wave vector values can be selected by applying an appropriate window function, and the other contributions will be filtered out. The applications of the technique include
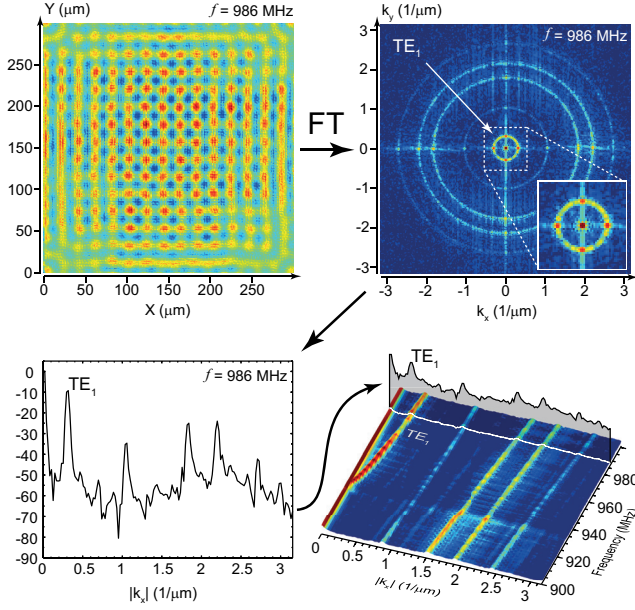
Figure 3.5. Illustration of the acquisition of a BAW dispersion diagram. The complex wave field data at a single frequency (f = 986 MHz) are Fourier transformed, and the FT result provides a modal decomposition of the measured wave motion (top right). In this case, the sample is a square ZnO thin film BAW resonator, and the symmetry due to the resonator geometry is clearly seen as, for example in the case of the TE_1 mode, the wave content is mostly localized to the x- and y-axes (bright red spots on the innermost circle, see the inset). In this case, it is feasible to extract the dispersion curves along one of the principal axes, dictated by the device and eigenmode geometry, e.g., along the x-axis ($k_y = 0$). This will result in slightly better dynamic range for the dispersion diagram, when compared to circular averaging of the FT result. The line data is further processed to yield a $|k_x|$-slice (bottom left), which contributes one line to the final dispersion diagram (bottom right).

selective visualization of certain wave modes of interest in BAW devices, separation of waves traveling to different directions and enhancing the dynamic range of the measurement by suppressing noise. Figure 3.6 illustrates the principle of selectively visualizing the amplitude field in a BAW resonator, including only the wave mode contributions from the $|\mathbf{k}_\parallel| = 0$ and TE_1 wave modes. In the example, the faint grid-like pattern in the original measured amplitude image, originating from modes with higher-$k_\parallel$, is removed while preserving the mode pattern and amplitude of the low-$k_\parallel$ contributions (see Fig. 3.6 (a) vs. (b)).

As a practical example, the technique was utilized to lower the noise floor in our first measurement results regarding BAW transmission properties of an acoustic mirror presented in our conference paper [85] and as a part of data presented in an invited paper [86]. The filtering was
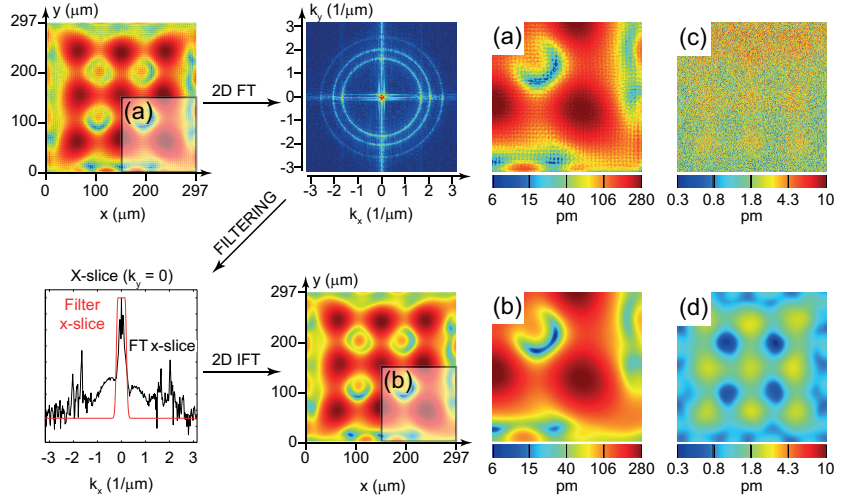
Figure 3.6. Illustration of filtering the vibration amplitude profile (f = 936 MHz) in the wave-vector domain. First row: the figure shows the original amplitude field measured on top of the resonator and the magnitude of the FT showing all the wave content. Second row: x-slice of the FT, together with the window function used for filtering. Only the x-slice is shown for the sake of clarity. The filtering removes all the high-$k_{\parallel}$ components, leaving only the $|\mathbf{k}_{\parallel}| = 0$ and TE_1 components unaltered. Filtered image shows the same overall pattern as the original, but the ripple has been eliminated. (a) presents a close-up-view of the original wavefield amplitude image and (b) the amplitude image after FT-filtering. (c) presents a measured weak amplitude field of BAWs transmitted through an acoustic mirror and (d) shows the amplitude field of the same data after FT-filtering.

applied to aid visualization of the weak wave fields leaking through the acoustic mirror. The filtering removes both the noise and the signal outside the selected wave-vector range, thereby allowing for an increased dynamic range of the measurement at the cost of visualizing only the selected wave modes. In studying the mirror transmission properties, the most interesting contributions, in terms of the visualization, were those close to the $|\mathbf{k}_{\parallel}| = 0$ (including the TE_1 mode branch). Hence, much of the wave vector space can be filtered out, thereby significantly reducing the noise level, as can be seen by comparing Fig. 3.6 (c) and (d).

4. Surface acoustic waves

After the invention of the IDT, surface acoustic waves have been widely utilized in a variety of signal processing applications, such as high performance filters for mobile communications, delay lines, sensors, and RF-identification tags [87–89]. Despite the seemingly simple structure to launch and receive SAWs, and the relatively straightforward manufacturing process, the design of SAW devices is demanding. Piezoelectric substrates are anisotropic by nature, and hence, wave excitation and propagation properties have directional dependencies. Typically SAW devices are manufactured on wafers of particular cuts of a piezoelectric single crystal, such as $LiNbO_3$ or $LiTaO_3$. The supported wave modes and their properties depend on the material and the crystal cut. A schematic illustration of a basic SAW device structure is provided in Fig. 4.1.

Research and development of SAW devices strives towards high-Q devices with low losses and with a clean frequency response, devoid of spurious resonances. Apart from these generic needs, recent research and development has also addressed the need for materials and structures to provide compensation for the temperature dependence of the frequency response. Furthermore, a surface acoustic wave is very sensitive to surface perturbations and, therefore, SAWs can be used to construct extremely sensitive sensors [89–91]. On the other hand, the use of SAWs in other applications, such as in filters, typically requires hermetic packaging so that the environmental conditions can not alter the wave propagation properties. With the development of ever smaller and multifunctional mobile communications devices, there is a demand to reduce the size of the filter components, and hence there is a need to reduce the size of the package, or to remove it altogether [92]. To enable components without packaging, boundary waves are studied as a potential candidate for high-performance, temperature compensated chip-size components [93, 94].
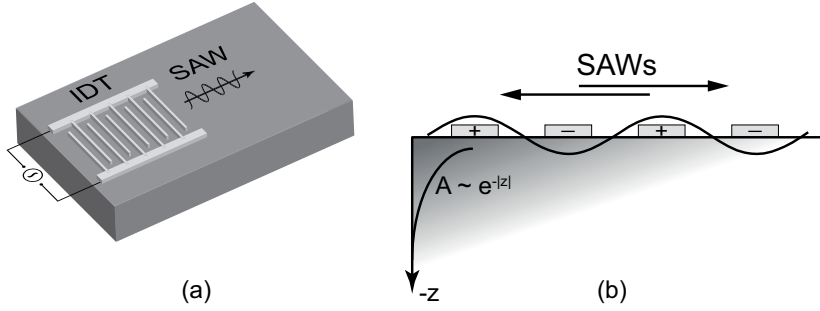
Figure 4.1. Illustration of the electrical excitation of SAWs via an interdigital transducer on a single crystal piezo-electric substrate. (a) Electrical excitation signal connected to the metal electrodes that form a finger structure (IDT) on the crystal. (b) Cross sectional view of the IDT structure with the instantaneous alternating electrical potentials ($\pm$) shown on the electrodes. The (basic) IDT structure launches waves into both directions. The SAW is confined to the vicinity of the surface and the wave amplitude decays exponentially into the depth of the substrate.

Recently, significant research effort has been devoted to phononic crystals (PnCs), one-, two-, or three-dimensional periodic structures that consist of two (or more) materials with different elastic constants giving rise to stop bands, or band gaps (BGs), for acoustic wave propagation in the material [95–98]. These engineered, artificial, metamaterials hold the potential for tailored wave propagation properties for acoustic wave devices, alleviating the constraints of only having a set of naturally occurring materials with fixed propagation properties to work with. An example of an artificial PnC material for confining elastic energy and enabling control of the dispersion of the waves is described in Ref. [99].

In the research and development of SAW devices, simulation tools such as finite element method (FEM) or the coupling of modes (COM) model, based on numerical and analytical methods, respectively, are vital for successful device design. The physics and the propagation properties of SAWs have been extensively presented in several papers and books [100–104]. Due to the complexity of the coupled electrical and mechanical waves and wave propagation in anisotropic media, the simulation tools and the modeling have their limitations. Numerical modeling has progressed to a point where it may be used to solve some of the practical device geometries [105–107], but for many applications a full multiphysics-FEM treatment is still too demanding in terms of memory and computing power required. In practise, this leads to the use of simplified models for device

design instead of a complete multiphysics treatment. Experimental characterization of the devices is therefore needed to validate the modeling and to verify the correct operation.

Because the performance of the end-product is determined by the electrical response, the experimental characterization of SAW devices has mainly consisted of electrical measurements. Vector network analysis enables accurate characterization of the electrical performance, but despite its merits, it often can not reveal the actual underlying mechanical processes that lead to the electrical response. Since the device operation is based on the electromechanical response, it is of considerable interest to be able to directly characterize the mechanical behavior of a SAW device. A particularly successful example of the merits of laser interferometry in the characterization of SAW devices is the discovery of a significant new loss mechanism for leaky-SAW resonators [108]. With the aid of the experimental data, the effect was then later theoretically explained [109, 110]. It is expected that the experimental characterization of the vibration fields is especially beneficial for the research and development of PnCs, where it is particularly challenging to characterize the wave interaction with the complex micro and nano structures.

A phononic crystal for SAWs at 200 MHz range [111], showing unexpected behavior in electrical measurements, was interferometrically characterized and the results reported in Publication II. In contrast to the typical PnCs exploiting a regular arrangement of scatterers, Publication III presents interferometric measurements of a random ripple pattern due to multiple scattering of SAWs from a large ensemble of random scatterers. Fourier transform techniques are utilized to unveil the complete slowness curve of SAWs without any prior knowledge on the wave propagation.

4.1 Phononic crystal for surface acoustic waves

Recently, PnCs and elastic stop bands for SAWs have been at the center of a growing research effort [112–116], both because of interesting wave physics involved and due to potential for significant impact on technological applications. Since the SAWs are by nature confined to the vicinity of the surface, a lithographically defined, two-dimensional PnC is, in principle, able to provide full-confinement of the waves. This is an interesting technological aspect, as fabrication of a true three-dimensional metama-
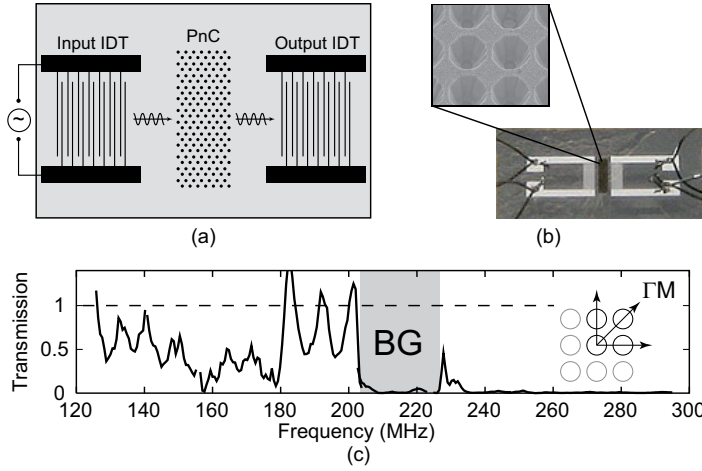
Figure 4.2. Phononic crystal structure for SAWs. (a) A schematic presentation of the test structure, a SAW delay line with a PnC structure in between two IDTs, intended to facilitate characterization via electrical measurements. (b) Photograph of the component and a closeup SEM image of the PnC hole structure etched into the $LiNbO_3$ single crystal substrate. The photograph shows bond wires providing electrical connections to the IDTs via busbars and the PnC hole structure in between the two IDTs. (c) SAW transmission characteristics determined via electrical measurements. The BG frequency range is indicated with a gray shading.

terial is not needed. Furthermore, the design of SAW devices has been somewhat limited by the availability of piezoelectric single-crystal materials and cuts with favorable properties. The possibility to utilize PnC structures to engineer new materials properties and sophisticated transfer functions for microacoustic components is therefore desirable for the industry.

Experimental demonstrations of micrometer scale PnCs in piezoelectric crystals, creating directional [117] as well as full BGs [111] have been reported. These studies have utilized the possibility to generate and receive SAWs using IDTs, and hence, to characterize PnCs in device test-structures via electrical measurements. Despite the relative simplicity of electrical measurements, they provide only indirect and partial information on the wave propagation and interaction with the PnC. In addition, generation and detection of ultrasound by picosecond laser techniques has been utilized to measure SAW dispersion properties in one- and two-dimensional PnCs [62,63]. Although the technique is well-suited for the characterization of PnCs in various geometries without the need for electrical excitation of the waves, the frequency resolution is typically somewhat limited.
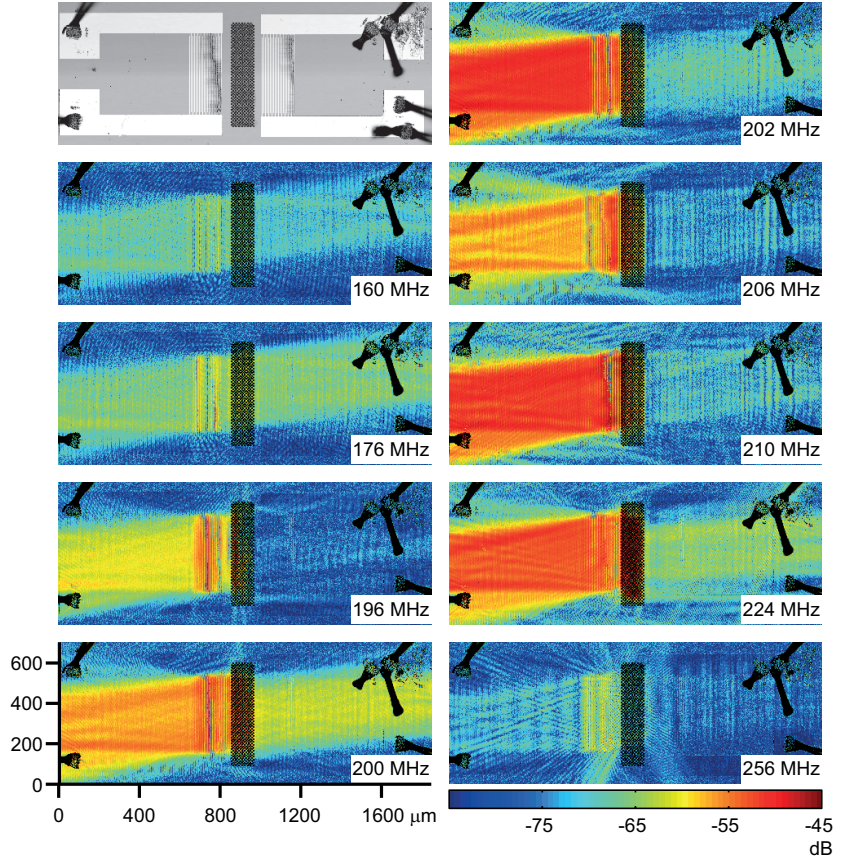
Figure 4.3. Light power image and measured wave field amplitude images at selected frequencies to show the acoustic behavior in the PnC device. Below the BG (160 and 176 MHz), the wave amplitudes, on both sides of the PnC structure, are similar, indicating a good SAW transmission. In contrast, within the BG frequency range (202-224 MHz), the PnC is very reflective, resulting in a strong standing wave pattern on the left side (input) of the PnC. This behavior is accompanied by a low transmission leading nearly to an absence of wave amplitude on the other side of the PnC structure. Above the BG frequency range, and above a threshold frequency, the PnC acts as an anisotropic diffraction grating scattering the incoming SAW field and producing an X-shaped amplitude pattern seen in the data at 256 MHz.

In previous work [111], a micrometer scale PnC structure has been studied in an electrically excited device configuration, with the intention to characterize the transmission properties of the PnC via electrical measurements. The device features a simple SAW delay line structure, with a PnC consisting of a 10 μm-pitch square lattice of 9 μm diameter, 10 μm deep air-holes etched into a single crystal LiNbO$_3$ substrate [118]. The PnC is placed in between two IDTs, see Fig. 4.2(a) for illustration and (b) for photograph of the device and a closeup of the hole-structure. This

device geometry allows to fabricate reference devices without the PnC and to compare the measured electrical responses in order to study wave transmission properties and the effect of the PnC on the electrical frequency response. For each propagation direction of the first Brillouin zone (ΓX, ΓY and ΓM), two sets (one with and one without the PnC) of 8 devices were needed to cover the frequency range of interest. The wave transmission characteristics for ΓM, determined from the electrical measurements, are shown in Fig. 4.2(c) [111], with a schematic presentation of the PnC geometry as an inset. The electrically determined wave transmission characteristics indicate a nearly complete suppression of signal around 215 MHz, coinciding well with the theoretically predicted BG frequency range (175-230 MHz). Above this frequency range, a re-transmission of waves is expected, but the experiment [111], shows little to no transmission after a small re-appearance of signal at around 230 MHz. This was contradictory to the theoretical predictions. SAWs scattering and coupling to the bulk modes of the substrate, due to the finite hole depth (slightly less than the acoustic wavelength) together with the conicity of the holes, were proposed as an explanation for the lack of re-transmission.

Due to the interesting, and partly unexpected, wave behavior observed in the previous study, the ΓM-oriented PnC structure was chosen for a further characterization of the SAW fields with laser interferometric measurements. An efficient transmission of SAWs through the PnC was observed at several frequencies below the BG frequency range. For example, at 160 and at 176 MHz, the SAWs pass through the PnC virtually without attenuation (despite the good transmission, note the small lateral shift of the SAW beam), see Fig. 4.3. As the electrical measurements suggest, the behavior is not entirely ideal, as the SAW transmission is actually frequency dependent also below the BG. The wave field measurements confirmed that within the BG-frequency range determined via electrical measurements the PnC is very reflective, not allowing SAW propagation through the crystal, thus experimentally confirming the existence of the BG for SAWs around 215 MHz, see the amplitude data at 202, 206, and 210 MHz in Fig. 4.3. Above the BG frequency range a re-transmission of SAWs is expected, but according to the electrical characterization, there is virtually no signal transmission after a small re-appearance of the signal at around 230 MHz. The wave field measurements reveal that after an onset frequency (theoretically 248 MHz) the PnC acts as an anisotropic diffraction grating. As a result, most of the SAW energy is not received by

the output IDT, and furthermore, the wave field at the output IDT has a lobe structure (as a result of wave interference) causing a mismatch with the IDT geometry, further reducing the received electrical signal. The measurement therefore revealed an effect not considered before, which provided explanation for the findings in the electrical measurement. This showcases the usefulness of optical characterization of wave fields in the research of novel microacoustic devices.

4.2 Wave slowness from random SAW fields

The anisotropic nature of the SAW crystal cuts influences the propagation properties of the acoustic wave, such as wave velocity, and in general makes the parameters angle dependent. Experimental determination of the wave slowness, $s = v^{-1}$, as a function of propagation angle on a substrate, is necessary for example when studying new materials for SAW applications. For this purpose, techniques using a phase-sensitive laser probe have been demonstrated. Wickramasinghe and Ash used a phase-sensitive laser probe to acquire two line scans of the transverse complex-valued field distributions that are a known distance apart to find out the portion of the slowness curve corresponding to the angular emission range of the SAW source [119]. This line scan method has been used together with angular spectrum theory to characterize both the slowness and wave attenuation [15]. On the other hand, time-domain optical pump-probe characterization has been used for spot excitation of waves and observation of the resulting ripples on the crystal surface [63]. It has been demonstrated that a few acoustic wave lengths away from the source, the phase front follows the shape of the surface wave, i.e., the locus of the group velocity as a function of the propagation angle. Scanning acoustic force microscope has also been utilized to observe the phase velocity of surface waves [46]. It has also been observed that the waves scattered from the edges of a sample can contribute to the measurement, although very faintly [120].

The prerequisite for the measurement of the complete slowness curve for SAWs is wave propagation to all directions in the surface plane. The wave excitation can be achieved by utilizing IDTs transmitting to all directions, such as an annular-IDT [121], or an IDT consisting of a few concentric fingers [122]. Another approach is to scatter an oncoming SAW beam such
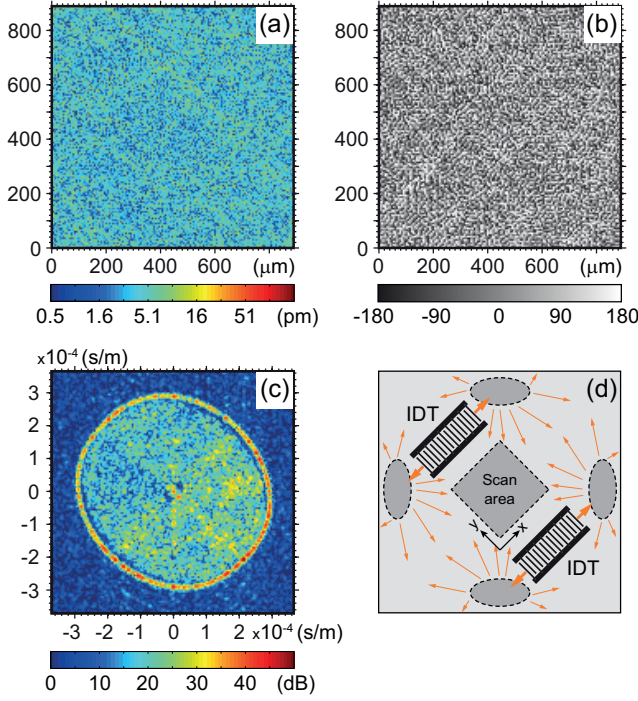
Figure 4.4. Measurement of a random SAW field and the extraction of the slowness curve of $LiNbO_3$ for SAWs. For comparison to calculated data, see Ref. [124]. The measured absolute amplitude and phase (in degrees) of the surface vibration field (at $f = 223$ MHz) are presented in (a) and (b), respectively. The Fourier transform of the measured surface vibration field in (c) shows a decomposition of the measured superposition of waves in the wave-vector space as a function of slowness (the inverse of the phase velocity). The measurement geometry is schematically depicted in (d).

that the scattered wave field features waves propagating to all directions in the surface plane, for an illustration see Fig. 3.3(b) and (c). In our experiment, described in Publication III, the SAWs are excited on Y-cut $LiNbO_3$ wafer by conventional IDTs with straight fingers and the SAW beams are directed towards areas that contain scattering structures, with random features smaller than the acoustic wavelength at the operation frequency. These structures are expected to scatter the waves such that there is wave propagation into all directions [123] within the measurement area, which is placed away from the direct SAW beams from the IDTs and into the far field of the scatterers.

The phase-sensitive heterodyne scanning laser interferometer (Publication I) is used to measure the resulting wave field. The scan area is situated away from the source-IDTs and from the scatterers, see Fig. 4.4(d). The scan area is $\sim 890 \times 890$ μm^2 and the scan step is 6.05 μm, while

the acoustic wavelength is ~ 16 μm, resulting in scans of 148×148 data points. The structure was characterized at several frequencies near the resonance frequency of the IDTs. Selected results at 223 MHz are presented in Fig. 4.4(a-c).

The measured wave field (both in amplitude and phase) within the scan area looks random, and without significant beam-like features, as intended. Despite the random look of the wave field, all the information of the wave propagation is in the data, and can be extracted by applying FT to the measured complex-amplitude wave field. The FT provides a decomposition of the wave field to plane-wave components, and allows to determine the wave content in the wave-vector space (k_x, k_y), where $|\mathbf{k}| = 2\pi/\lambda$. Since the wave velocity, wavelength and frequency are related by $\mathbf{v} = f\lambda$, the wave-vector is directly proportional to the wave slowness at a fixed frequency, $\mathbf{s} = \mathbf{v}^{-1} = \mathbf{k}/2\pi f = \mathbf{k}/\omega$. Therefore, the slowness curve for SAWs can be directly extracted from the measurement data via FT methods.

The FT result (Fig. 4.4(c)) is also a random quantity, but its amplitude is concentrated mostly along a closed curve in the wave-vector (Fourier) space. This closed curve is the slowness curve for the SAW propagation on the crystal surface. In addition, it is readily observed that inside the slowness curve, there is a disk filled with a random background of significant amplitude. In contrast, outside the slowness curve the FT amplitude is extremely low, corresponding to the noise floor of the measurement and indicating the absence of propagative wave modes. The filled interior of the SAW slowness curve is attributed to the waves that are scattered to the bulk of the crystal (substrate), and are trapped between the two surfaces of the wafer. These waves can propagate at any angle, but the projection of their wave vector in the surface plane is limited to that of the slowest bulk acoustic wave ($v_{\mathrm{BAW}} > v_{\mathrm{SAW}}$), as they are constrained to the sound cone. Furthermore, it is to be noted that the experimental data also show a gap, or 'forbidden' region between the SAW slowness curve and the interior filled disk.

The experimental results and the slowness curve computed using materials parameters for $\mathrm{LiNbO_3}$ [14] are in good agreement. The simulations also predict a gap between the calculated projection of the sound cone for the bulk waves and the slowness curve for the SAW, as observed experi-

mentally (see Fig. 2 (c) and (d) in Publication III). The granular appearance of the FT result is in accordance to the scattering theory presented in Publication III, where the singularity of the spectral Green's function enhances locally the speckled appearance of the FT result, hence rendering the slowness curve visible. Furthermore, the experimental wave field data are windowed (with a circularly symmetric Hann window [125]) before the FT, which increases the observed grain size in Fig. 4.4(c).

The random looking amplitude and phase fields together with the fairly uniformly colored closed curve in the FT result indicate that the scattering structures scatter the SAWs effectively into all possible angles of propagation (in-plane), which was the original intention. It is, however, surprising that in addition to the randomly scattered SAWs, waves are also scattered into the bulk with nearly all possible wave-vector values, as is evident from the rather uniformly filled speckled disk inside the SAW slowness curve.

The wave-vector (or slowness) resolution of the measurement can be roughly estimated from the ratio of the acoustic wavelength versus the scan dimensions, and can be improved by having a larger scan area. In our demonstration of the concept, the experiment was not optimized, and the relative resolution is estimated as $\lambda/\Delta x \approx 2\,\%$. Furthermore, when extracting numerical values for the slowness, function fitting can be utilized to determine the exact location of the slowness curve in the FT space enabling sub-pixel accuracy.

5. Bulk acoustic waves

Bulk acoustic wave propagation in solids is widely used for frequency reference and filtering applications. Perhaps the best known application is the quartz reference oscillator developed for high-stability frequency references utilized since 1920s [126]. The operation of the quartz crystal resonator is based on bulk acoustic wave resonance within a piezoelectric crystal plate, whenever an integer number of half an acoustic wavelengths fit within the effective plate thickness. For an illustration of a basic resonator structure, see Fig. 5.1(a). Quartz crystal resonators can be manufactured to have very low losses, i.e., with a very high Q-value (of the order of 1×10^6 at 15 MHz [127]), and with good temperature stability, which has resulted in their success in frequency and timing applications [128]. The fabrication of the crystal resonators relies on dicing thin plates from bulk crystals, and grounding and polishing them down to the desired thickness. Since the bulk wave mode velocity in the solid is determined by the elastic constants of the solid, the frequency of the fundamental resonance can be selected by manufacturing crystals of appropriate thicknesses. In other words, the dimensions of the plate and material properties of the particular crystal cut determine the resonance frequency of the crystal resonator. Manufacturing thin crystal plates is challenging, thereby limiting the applicability of quartz crystal resonators for frequencies below ~ 200 MHz [129].

Microfabrication techniques originating from microelectronics industry enable the deposition of various materials in the form of thin films on a range of substrate materials such as silicon or glass. The technology enables also the deposition of thin films of piezoelectric materials, such as ZnO and AlN, and metal electrodes, as well as patterning the structures into devices via lithography and etching. The use of thin film technology allows to manufacture piezoelectric resonators with sub-micron
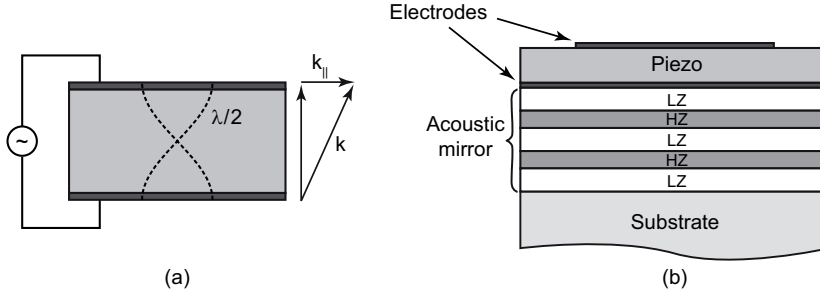
Figure 5.1. (a) Schematic view of a basic bulk acoustic wave crystal resonator. The longitudinal, fundamental, vibration mode, with approximately half of an acoustic wave length within the volume of the resonator and electrodes, is illustrated with dashed lines. The wave vector for purely longitudinal vibration is perpendicular to the surface, but in a general case, it is tilted giving rise to a lateral component $\mathbf{k}_{||}$. (b) Cross sectional view of a solidly mounted BAW resonator depicting the thin film layer stack. Depending on the component, one or several of the layers may be patterned. In contrast to the crystal resonator depicted in (a), in a SMR the resonator is acoustically isolated from the substrate by an acoustic mirror consisting of alternating layers of high (HZ) and low (LZ) acoustic impedances.

layer thicknesses, resulting in acoustic resonance frequencies in the GHz-range.

In order to produce a high-performance resonator, the acoustic energy has to be confined within the resonator, and hence, the thin film BAW resonator has to be acoustically isolated from its surroundings, such as the substrate. One way to achieve this isolation is to remove the substrate (or a sacrificial layer) beneath the resonator, creating a membrane type (FBAR) resonator. Alternatively, thin film processing may be utilized to deposit alternating layers of materials of high and low acoustic impedances to produce an acoustic Bragg reflector (see illustration of the structure in Fig. 5.1(b)), as suggested by Newell already in 1965 [130]. In these solidly mounted resonators (SMR), the acoustic mirror effectively isolates the resonator from the substrate.

5.1 Current trends in BAW resonator research

Research and development of BAW resonators strives towards resonators with high Q-values and with a clean electrical frequency response, devoid of spurious resonances [131, 132]. High-performance resonators enable filters with better performance, e.g., with steeper transition from pass-band to stop band, high out-of-band suppression, and lower insertion loss. One of the advantages of the filters based on BAW technology over the

competing SAW technology has been the greater Q-values [131]. The development towards higher Q-values, however, directly implies a need for a better control of energy losses in the resonators. The energy loss in a BAW resonator may be divided into losses of electrical and of acoustical (mechanical) origin. Electrical losses are due to, e.g., resistive losses in the electrical connections and metal layers. In the case of SMR-type resonators, two major sources of losses of acoustical or mechanical origin are the possible leakage through the acoustic mirror and the lateral leakage from the resonator area. Extensive research effort has been devoted to further the understanding of the dominant loss mechanisms, i.e., the limiting factors for obtaining high-Q resonators [133, 134].

A typical SMR-type BAW resonator is intended to operate with a longitudinal bulk wave mode, with no or very little lateral wave-vector component, and hence, the operation and the acoustic thin-film mirror is often modeled utilizing a one-dimensional transfer matrix model [135] for the longitudinal wave behavior in the thin-film layer stack, which is considered laterally infinite. The 1D transmission line model can be utilized to separately compute the mirror reflectivity for both longitudinal and shear waves by using the appropriate propagation parameters for each wave type.

For the SMR-type resonators, the mirror is central for achieving high performance devices. Ignoring all other loss mechanisms, losses through the mirror then define the maximum obtainable Q-value of the resonator, the mirror-limited Q. Since the Q-value of the resonator is one of the three most important basic parameters [132], the mirror optimization is of fundamental importance in SMR BAW resonators. Although the origin of losses in a BAW resonator can be divided into electrical losses, acoustical attenuation and leaking waves, the quantification of the losses, and hence their practical limiting effect, is difficult [132, 136].

The importance of the mirror design was emphasized by the work of Marksteiner *et al.* [136], where the authors challenged the standard practise of reflector design, in order to further improve the Q-value of resonators. A mirror optimized to provide maximum reflectivity for longitudinal waves, the intended operation mode, a so called quarter-wave, or $\lambda/4$, mirror, does not provide effective energy confinement for shear waves, but rather allows most of the shear wave energy to leak through [137]. Despite the vertical excitation geometry and the intended purely longitu-

dinal mode of operation, the SMR BAW resonators support wave modes with shear component in order for the waves to fulfill the boundary conditions in the device layer stack. Marksteiner *et al.* showed that with a particular $\lambda/4$ mirror, leading to $Q_{\mathrm{long}} \sim 30\,000$ for longitudinal waves and $Q_{\mathrm{shear}} \sim 10$ for shear waves, if just 1% of the total energy is converted to shear waves, the total quality factor drops to $Q_{\mathrm{tot}} \sim 970$. Thus, a small amount of total energy in shear waves results in a dramatic loss of Q_{tot}. The authors experimentally verified their assumptions and measured resonator Q values at the parallel resonance (Q_p) from a resonator with a standard $\lambda/4$ mirror, resulting in typical $Q_p \leq 500$, and from an optimized design, where some of the reflectivity for the longitudinal waves was sacrificed to get shear reflectivity, having $Q_p \sim 2\,000$. This significant improvement in Q_p indicates that at this performance level the dominant loss mechanism of the longitudinal mode operated SMR BAW resonator was actually due to shear wave losses through the traditional $\lambda/4$ mirror. This significantly changed the view of the operation of the SMR BAW resonator, and serves also to emphasize the importance of experimental verification of the validity of the commonly used models and the various assumption and simplifications. Further investigations have been conducted on resonators utilizing the optimized mirror, to see if there still remains a significant mirror loss, by removing the substrate from underneath the SMR-resonators [138]. The study showed that there is still some energy leakage through the optimized mirror, but this is not anymore the dominant effect limiting the resonator Q-value.

Publication IV addresses the need for experimental characterization of the performance of the acoustic mirror by further development of laser interferometric data analysis to quantify the actual SMR mirror transmission properties. Detailed wide frequency range interferometric measurements are utilized in connection with Fourier transform techniques to relate the experimentally determined acoustic behavior with the simulation results. The extensive data allows to evaluate the validity of the commonly utilized modeling tools.

To be able to actually use the resonators in filtering applications, it is essential for the resonator to have a clean electrical frequency response. The desired high Q-value reveals any unwanted spurious resonances in the electrical response. The detrimental spurious resonances in the electrical response have been attributed to the lateral standing wave resonances

arising in the finite-sized resonators [132, 139]. To solve the problem of lateral standing wave resonances leading to contamination of the electrical response, several approaches have been suggested, such as utilizing random or oval-shaped resonators to avoid the lateral standing wave resonances [140, 141]. It has also been claimed that regardless of the shape of the resonator, pronounced spurious resonances will arise when $Q > 1\,000$ unless special measures are applied to suppress them [131]. Perhaps the most successful solution is to design a frame region around the active area of the resonator, in order to suppress the (electrical) coupling of the lateral standing wave resonances by appropriately modifying the boundary condition [139]. A successful implementation of this design requires an accurate knowledge of the plate wave dispersion properties of each of the acoustic regions, a task for which interferometer measurements are advantageous.

Prior to the research described in this thesis, there had been no direct proof that the lateral standing wave resonances are indeed responsible for the spurious electrical responses, although this is a theoretically feasible explanation. In our preliminary studies for Publication IV, published as conference articles [85, 142], we included a comparison of the electrical power absorbed in the resonator to the mechanical response of the resonator obtained from a measured dispersion diagram as a function of frequency. The comparison shows a good qualitative correspondence between the electrical and mechanical responses, an experimental result, which has been considered to 'verify the theoretical reasoning' of the origin of the spurious electrical responses [132].

Publication V refines this concept further by presenting an experimental method for selective characterization of the lateral eigenresonances of the TE_1 mode. This is accomplished by following the selected mode branch in the dispersion diagram and plotting the wave amplitude as a function of frequency. The described method allows to study and extract detailed information of the individual eigenresonances.

Publication VI reports a way to extend the dispersion measurement to the sourceless outside region of the resonator and introduces a method for direct experimental characterization of the lateral energy trapping frequency range. Apart from a direct view on the resonator physics, the technique also enables to measure the dispersion properties of the various acoustic regions.
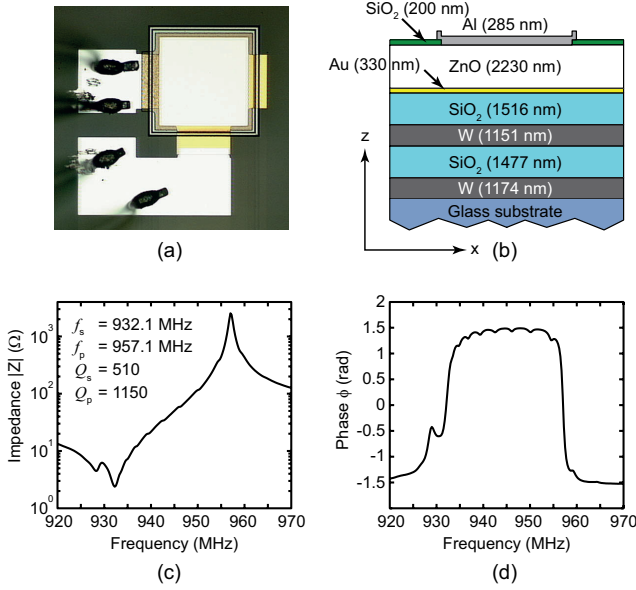
Figure 5.2. Photograph, thin-film layer stack and wafer-level electrical measurements of a 932 MHz solidly mounted BAW resonator. (a) Photograph, (b) schematic presentation of the thin-film layer stack, (c) impedance and (d) phase of the measured electrical response.

Publication VII extends the measurement of the dispersion properties of the sourceless region further to include also the dispersion of the evanescent part of the TE_1 mode branch in the outside region.

5.2 Transfer characteristics of the acoustic mirror

Publication IV presents a comprehensive study of the dispersion and mirror transfer properties of a solidly mounted BAW resonator. The study introduces a direct experimental way to measure the transfer characteristics of an acoustic mirror via laser interferometric measurements. The extensive experimental data are compared to the predictions by the commonly used 1-D and 2-D simulations.

Conventionally, the interferometric measurements have been performed on top of the resonator only. By turning the component upside down, the wave fields can be measured also on the back side of the sample, either the far field pattern from the bottom of the wafer [77, 143], or in the case of a transparent substrate material, such as glass wafer, on the interface between the bottom of the mirror stack and the glass substrate. This approach allows to obtain information on the waves leaking through the mirror.
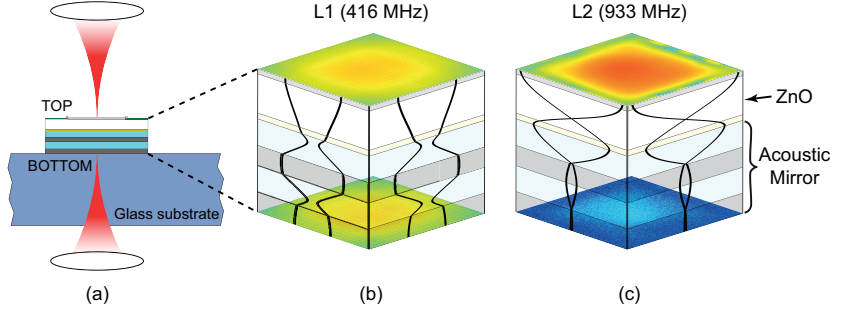
Figure 5.3. Illustration of the measurement principle used in Publication IV. (a) Cross sectional view on a solidly mounted BAW resonator, with laser beams indicated as focused on top of the resonator and at the bottom of the acoustic mirror. (b) Measured amplitude distributions (2D), both on top of the resonator and on the bottom of the acoustic mirror, together with the layer stack and simulated (1D) displacement profiles for the longitudinal (L1) mode. This longitudinal resonance is not confined to the resonator area, but extends throughout the layer stack (see the 1D profile) and therefore the measured amplitude values and the shapes of the distributions are similar. (c) Measured amplitude distributions (2D), both on top of the resonator and on the bottom of the acoustic mirror, together with the layer stack and simulated (1D) displacement profiles for the fundamental longitudinal thickness extensional (TE_1, L2) mode. This is the principal operation mode of the resonator and the vibrations are well confined within the volume defined by the piezoelectric ZnO-layer and the top- and bottom-electrodes. Therefore, the measured amplitude field at the bottom of the acoustic mirror is significantly attenuated (blue color) as compared to that on top of the resonator (red).

To characterize the operation of the acoustic mirror in a 932 MHz solidly mounted ZnO-based BAW resonator (see Fig. 5.2 for sample details), the wave fields were interferometrically measured both on top of the resonator and at the bottom of the acoustic mirror, at the interface between the last mirror layer and the glass substrate (see Fig. 5.3 for illustration of the measurement principle). The measurements were performed over a large frequency range, extending from 350 MHz to 1200 MHz (464 frequencies with a varied frequency step). Dispersion diagrams were calculated from both data sets and used to compare the wave content on the top and on the bottom of the device in the frequency-wave-vector space, enabling quantitative analysis of the transmission properties of the acoustic mirror for the different wave modes excited in the structure.

This approach is superior to just comparing the measured wave field amplitudes, since the mirror in general may have very different response for, for example, the purely longitudinal ($|k_\parallel| = 0$) and for the laterally propagating waves. Furthermore, because the measured wave field images are superpositions of the wave motion, it is difficult to come up with another way to compare them in a reasonable fashion. The use of Fourier transform techniques and dispersion diagrams solves this problem.

In addition, the dispersion diagram calculated from the measurement data on top of the resonator provides a wealth of information on wave mode excitation and wave propagation in the acoustic metamaterial composed of the thin film layer stack. Together with simulations, the measured dispersion diagram was used to identify the different wave modes (fundamental thickness extensional, TE_1 and first and second order thickness shear, TS_1 and TS_2), resonances and the onset frequencies of their dispersion branches.

Figure 5.3 presents examples of the measured surface vibration amplitude distributions (2D) on both sides of the resonator, together with the simulated displacement profiles (1D model) as a function of depth into the layer stack, corresponding to two selected features. The 1D model result shows the confinement of the energy of the principal operation mode, the longitudinal half-wave resonance (L2), within the electrodes and the piezolayer (the three topmost layers) and a strong attenuation provided by the mirror leading to almost an absence of displacement at the bottom of the mirror, see Fig. 5.3(c). In contrast, the wave mode of the longitudinal resonance L1 is not confined to the volume of the resonator, but extends throughout the layer stack. The 1D model therefore predicts a significant displacement also at the bottom of the mirror, a result supported by the experimental data, see Fig. 5.3(b).

Selected wave field amplitude images measured from the top and from the bottom of the resonator are presented in Fig. 5.4. The dispersion diagrams and the mirror transfer characteristics diagram (see Fig. 5.5), together with the wave field images are utilized to analyze the device behavior. The sample features a longitudinal wave resonance at $f_I = 416$ MHz, which is not confined to the resonator area, but rather extends throughout the device layer stack having a vibration maxima both at the top and bottom (as predicted by the 1D-model). This behavior is manifested in the measured wave field amplitude images as identical looking lobe structures with comparable amplitude values at $f_I = 416$ MHz in Fig. 5.4. The dispersion diagrams on top and at the bottom feature a resonance localized on the frequency axis ($|k_\parallel| = 0$), indicating a longitudinal nature of the wave mode. The resonance features similar amplitudes both on top and at the bottom, therefore resulting in a low attenuation (close to 0 dB) value observed in Fig. 5.5(c). This observed longitudinal resonance corresponds to the simulation result L1 presented in Fig. 5.3(b).

The second labeled amplitude image in Fig. 5.4, at $f_{II} = 448$ MHz, shows a peculiar behavior, where the amplitude at the top of the resonator is extremely low, whereas at the bottom there is a slightly larger amplitude. This frequency is identified in the dispersion diagrams as the first thickness shear (TS_1) wave resonance and the starting point of the mode branch. At the TS_1 resonance frequency the wave motion is confined in the surface plane without a vertical component, and hence can not be detected by the interferometer. There exists, however, also a longitudinal wave minimum, together leading to the low detected vibration amplitude at the top of the resonator and a slightly larger amplitude at the bottom. The corresponding behavior can be found in 1D simulations, predicting almost a vibration node on the top of the resonator with displacement maxima located within the resonator and the mirror stack.

The third labeled amplitude image in Fig. 5.4, at $f_{III} = 830$ MHz, is the second thickness shear resonance (TS_2). At the TS_2 resonance frequency, the wave motion is again confined in the surface plane and a pure shear wave is not detected by the interferometer. There is, however, simultaneously a significant longitudinal wave component present. The acoustic mirror is broadband enough to provide significant reflection to the longitudinal waves, and it does also provide some reflectivity for the shear waves, which leads to the low detected amplitude values at the bottom.

The fourth labeled amplitude image in Fig. 5.4, at $f_{IV} = 933$ MHz, is the fundamental thickness extensional resonance (TE_1), also a starting point of the mode branch. This corresponds to the longitudinal resonance L2 in Fig. 5.3(c). The acoustic mirror is optimized to reflect the longitudinal waves resulting in high attenuation values (up to $\sim$37 dB) observed for the longitudinal waves, see the wave content in Fig. 5.5(c) at the frequency axis ($|k_\parallel| = 0$).

The mirror transmission properties for the longitudinal waves are determined from the mirror transfer characteristics diagram, Fig. 5.5(c), by extracting a line profile along the frequency axis ($|k_\parallel| = 0$) and plotting it together with a corresponding result extracted from the 1D simulation as a function of frequency on the left hand side in Fig. 5.5(c). This provides an experimental determination of the attenuation provided by the acoustic mirror for longitudinal waves and is in a good agreement with the 1D simulation result.
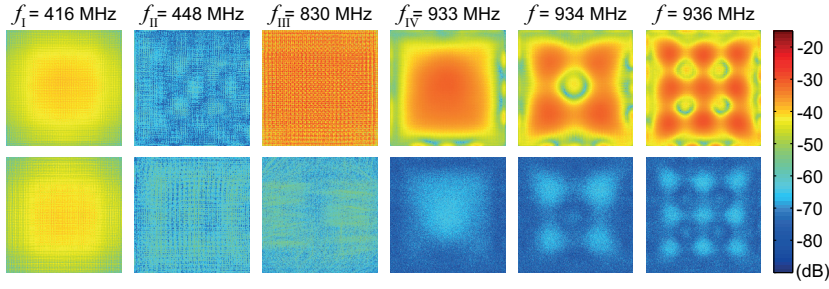
Figure 5.4. Selected vibration amplitude field images from 932 MHz ZnO solidly mounted BAW resonator. Top row: Amplitude images measured from the top of the resonator. Bottom row: Amplitude images as measured from the interface between the bottom of the acoustic mirror and the glass substrate.

As a conclusion, the results show a very good correspondence between the predicted displacement behavior and the laser interferometric measurements, both on top of the resonator and at the bottom of the mirror stack. The reported experimental method allows also to selectively study the mirror transmission characteristics for the longitudinal wave, and hence, enables a direct comparison to that predicted by the 1D model. Furthermore, a good correspondence is also found between the FEM-simulated and measured dispersion and mirror transmission properties.

5.3 Characterizing TE_1 eigenresonances

In Publication V we describe a method to study the mechanical response of the BAW resonator corresponding to a selected wave mode branch. To demonstrate the concept, the eigenresonances of the TE_1 mode branch of a 1820 MHz AlN resonator are studied in detail and compared to a multimode mechanical equivalent circuit model via function fit. The work addresses the need for advanced experimental methodology to study the lateral eigenresonances appearing in a resonator due to its finite size. These resonances have been attributed as the origin of the spurious electrical responses [85, 132, 142], often observed in high-Q resonators unless special care and measures are taken against them [139]. Although the spurious-free operation is one of the top priorities of a BAW resonator designer [132, 136], there have not been publications providing an experimental way to study the lateral eigenresonances of an individual wave mode.
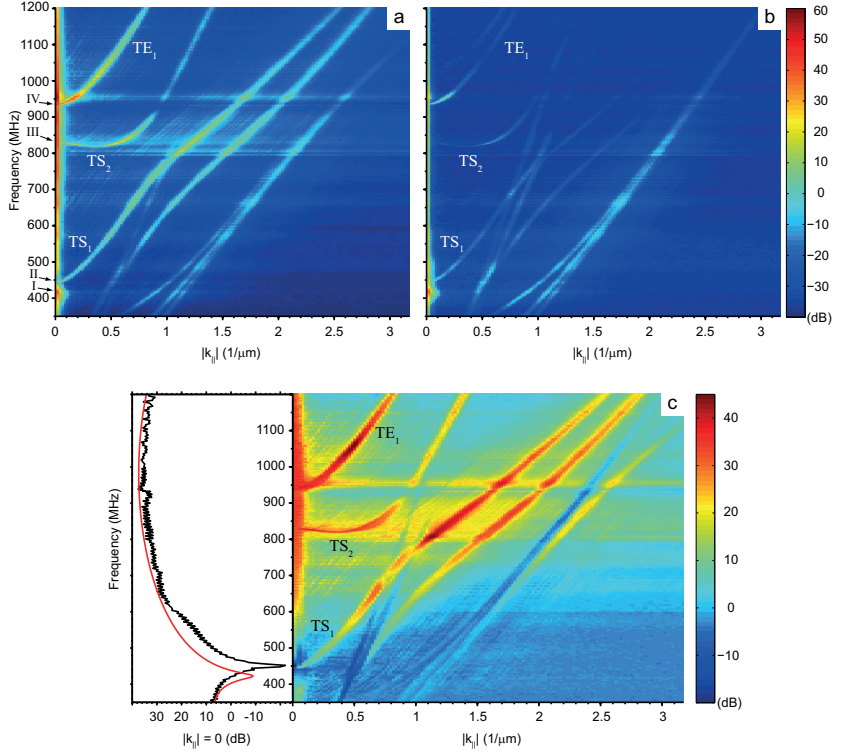
Figure 5.5. Dispersion diagrams obtained from the top of the resonator (a) and from the interface between the bottom of the acoustic mirror and the substrate (b) and mirror transfer characteristics calculated from the measured data (c). Mirror attenuation for the purely longitudinal waves, with $|k_\parallel| = 0$, is provided as a function of frequency, the black curve is extracted from the measurement and the red curve is the theoretical prediction according to the 1-D model.

The wave fields excited in a typical solidly mounted BAW resonator are superpositions of different wave modes, and as a consequence, the amplitude and phase images from the wave field measurements do not represent any of the single constituents alone. The characterization of the properties of lateral eigenresonances from the amplitude and phase images alone is therefore difficult. Publication V presents an alternative way to single out a desired wave mode and to study its properties by further utilizing dispersion diagrams, calculated from the data.

When measuring a BAW resonator with a high Q-value and of symmetrical geometry, lateral standing wave resonances are observed in the measured amplitude and phase field images. When a dispersion diagram is calculated from a high-quality data set with enough frequency resolution, a mode branch will be formed as a chain of discrete maxima instead of a constant wave amplitude (uniform color). The discrete maxima are the lateral eigenresonances arising in the resonator. Following the mode

branch and plotting the magnitude of the FT result as a function of frequency enables the extraction of information on the individual eigenresonances.

In the dispersion diagram, the frequency resolution is determined by the frequency step used in the laser interferometric measurement, while the resolution with respect to the wave-vector, $k_\parallel$, is determined by the size of the scanning area, and thus, typically by the size of the resonator. The windowing of the data, used before the FT, provides significant side-lobe suppression at the cost of widening the $k_\parallel$-peak in the wave-vector space [125].

The concept of characterizing the individual eigenresonances is demonstrated by measuring the wave fields in a 1820 MHz solidly mounted, circular shaped BAW resonator, see Fig. 5.6. The dispersion diagram, calculated from the data, features a TE_1 mode branch that consists of a chain of maxima, see insets 1 and 2 in Fig. 5.9. The TE_1 mode branch is followed and the magnitude of the FT is extracted as a function of frequency.

The electrical behavior of a multi-mode resonator is often presented with a modified Butterworth van Dyke (mBvD) equivalent circuit model with several resonance legs [132, 137, 144]. There is a mechanical analogue to the electrical circuit, where the current drawn by the circuit is proportional to the mechanical vibration amplitude, and can be expressed as

$$I(\omega) = \underbrace{j\omega C_0 V}_{\text{offset}} + \sum_{i=1}^{N} \underbrace{\frac{k_i^2}{1-k_i^2} C_0 Q_i \omega_i V}_{A_i} \underbrace{\frac{1}{1 + \frac{Q_i(\omega_i^2 - \omega^2)}{j\omega_i \omega}}}_{F_m(\omega)}, \qquad (5.1)$$

where C_0 is the static capacitance, a resonator-geometry-related constant that is independent of the eigenmode i, V is the driving voltage, k_i the electro-mechanical coupling coefficient, Q_i the quality factor and ω_i the angular resonance frequency of the eigenmode i. The shape of the resonance peak is determined by the part labeled $F_m(\omega)$, whereas the part labeled A_i is a mode-dependent constant. The first term can be regarded as a resonator-geometry-related offset. Fitting this equation to the data extracted from the dispersion measurement enables a quantitative characterization of the individual eigenresonances. In Publication V the technique is demonstrated by determining the properties of the 6 first eigenresonances of the TE_1 dispersion curve. The resulting function fit (crosses) is shown with the original data ($A_{TE_1}(f)$, solid black line) in Fig. 5.10(a) with 6 of the resonances labeled for comparison. The corresponding wave field amplitude distributions are presented in Fig. 5.7. The eigenfrequen-

cies f_i and Q-values Q_i for each resonance i were obtained from the function fit. Furthermore, the technique allows to also extract the relative coupling coefficients k_i of the eigenmodes via the fit parameter A_i, and in principle with normalizing and with further knowledge of the resonator, to also extract the absolute values of the coupling.

The excellent match observed between the function fit and the extracted TE_1 amplitude data indicate that the behavior of the lateral eigenresonances in the resonator can be described by a linear superposition of uncoupled eigenresonances. Additionally, if desired, the amplitude distribution corresponding to a single eigenmode may be visualized by utilizing Fourier filtering techniques. This technique, developed to isolate and study the mechanical responses of particular wave modes, was also utilized in Publication VI to show the plate wave dispersion properties of the active and outside areas of the resonator and their connection to the lateral energy trapping condition, the existence of the lateral eigenresonances and spurious electrical responses.

With a suitable sample, something similar might also be accomplished via electrical measurements, however, the technique presented above is superior in cases where the mechanical responses are separable (e.g., a rectangular resonator), but their electrical responses overlap. Furthermore, the technique could prove useful also in cases, in which the resonator edges have different layer structures, such as to study the effect of a boundary condition to the lateral eigenresonances in a square resonator with different edge structures in x- and y-directions.

5.4 Outside area dispersion and lateral energy trapping

In a BAW resonator, the mechanical energy needs to be confined not only in the vertical direction, but also in the lateral direction. The confinement in the vertical direction is accomplished by using an acoustic mirror (in SMRs) as discussed earlier. The confinement in the lateral direction can be achieved by tailoring the dispersion properties of both the resonator and the surrounding area such that at the resonance frequency, and in a sufficiently wide frequency range around it, the surrounding medium does not support propagative wave modes, but rather features evanescent waves. The concept has been presented and applied successfully earlier also in quartz resonator technology [127, 132, 137].
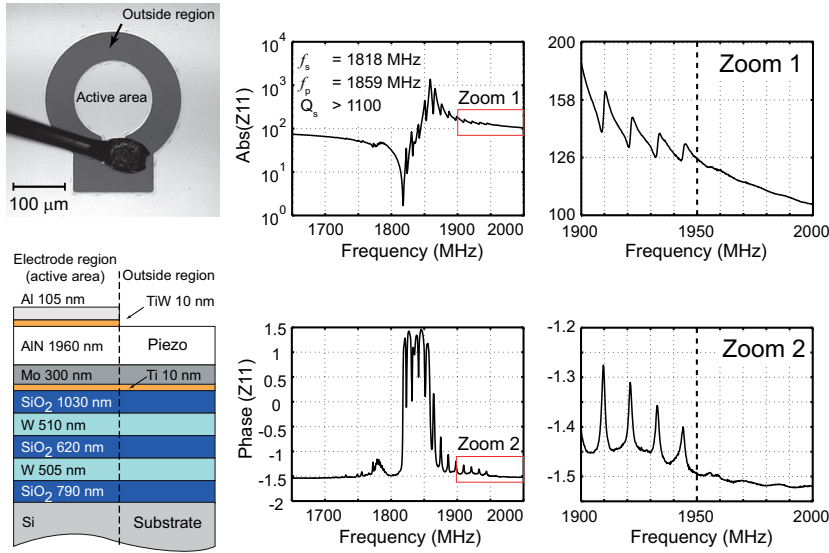
Figure 5.6. Photograph, thin film stack with measured (SEM) layer thicknesses and measured electrical response (on wafer) of a 1820 MHz thin film BAW resonator. The photograph shows the sample with the different acoustic regions labeled. Electrical measurements: Impedance and phase response obtained with a wafer-level measurement. Main figures of merit are provided as an inset. The electrical response features strong spurious resonances. Zoomed views to the impedance and phase response are provided to show the spurious resonances in detail and their sudden disappearance at around 1950 MHz.

Interferometric measurements of waves in the region outside of the resonator's active area are not new, as several authors have observed and reported waves leaking from the active area [77, 145, 146]. Fourier filtering techniques have also been utilized to visualize the amplitude fields due to waves with a lateral wave vector of interest [145, 146]. The frequency dependence of the leakage and the dispersion properties of the sourceless outside region, however, have not been previously characterized.

Publication VI presents an extension of the laser interferometric characterization of the dispersion properties to the sourceless region around the active resonator area. The concept is demonstrated using the 1820 MHz AlN resonator sample presented in Fig. 5.6. The measurement characterizes the waves leaking from the active resonator area and the concept is based on windowing the measurement data such that only the data from the outside area is effective in the Fourier transform, see Fig. 5.8. Significantly, we have now demonstrated that it is possible to characterize the dispersion properties both in the active area of the resonator as well as in the sourceless region around it. The new detailed information
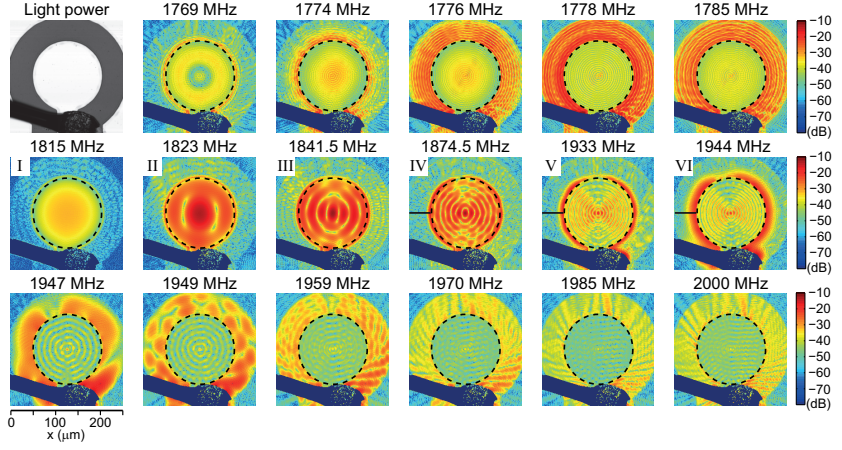
Figure 5.7. Selected amplitude images from a 1820 MHz AlN thin film BAW resonator, illustrating the acoustic behavior below (top-row), within (middle-row) and above (bottom-row) the lateral energy trapping frequency range. The edge of the active resonator area is marked with a dashed circle to guide the eye. The resonator is intended to operate within the lateral energy trapping frequency range, featuring large amplitude in the resonator and virtual absence of amplitude in the surrounding region which does not support propagative wave modes. In contrast, both below and above the lateral energy trapping frequency range, the surrounding outside region supports propagating waves and hence allows the resonator energy to leak to the surroundings. This is manifested as significant wave amplitude observed in the outside region. The features in the dispersion diagram corresponding to the labeled (I - VI) amplitude distributions are shown in Figs. 5.9 and 5.10. Taking a closer look at the amplitude data close to the upper cut-off frequency ($f_c = 1947$ MHz) at 1933 and 1944 MHz (V and VI), the displacement field in the resonator induces an evanescent wave into the surrounding outside region (seen as radially decaying amplitude away from the resonator edge). The location of the radial line outside the resonator used for evanescent wave dispersion determination is indicated with a black line in IV to VI.

will give valuable feedback to the device designer regarding whether or not the manufactured thin film layer stack behaves as expected. More importantly, in the case of laterally coupled BAW resonator filters [147, 148], the dispersion properties of the surrounding medium that couples the resonators is vital for correct device operation.

Furthermore, Publication VI shows a direct connection between the sudden diminishing of the lateral standing wave resonances, and the corresponding spurious electrical responses, with the cutoff frequency of the dispersion curve of the surrounding medium, see Figs. 5.6, 5.7, 5.9 and 5.10(a). The observation is in line with our earlier results [85, 142] and serves to further support the conclusion that the lateral eigenresonances are the origin of the spurious electrical responses [132] often observed in high-Q resonators. This experimental finding supports the theoretical
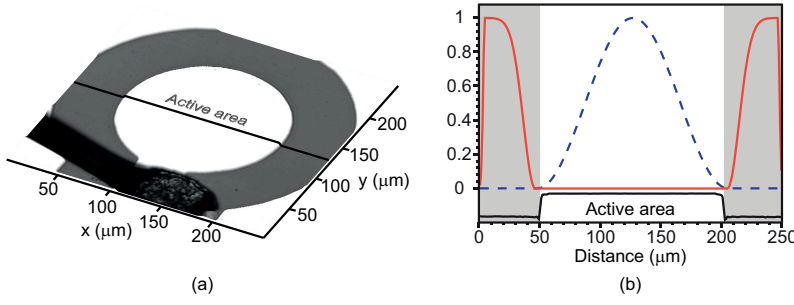
(a)　　　　　　　　　　　　(b)

Figure 5.8. Illustration of windowing the measurement data prior to FT for both the active area and for the outside area dispersion measurement. (a) Light power image of the scan area, with the resonator active area in the center. The black line indicates the location of the cross-sectional line presented in (b). (b) Cross-sectional lines of both circularly symmetric window functions applied to the data before active-area (blue dashed line) and outside-area (red line) dispersion calculation, together with an inset to compare with the corresponding light power profile (black line). The active resonator area is selected by applying a centrosymmetric Hann window that goes smoothly to zero outside the active area. The outside area (indicated in (b) with gray shading) is windowed such that the window is forced smoothly to zero (gaussian edge) for the active area, as well as at the edges of the data.

understanding of the wave behavior and provides a unique direct experimental view on the device physics.

Ideally, one should be able to characterize the wave dispersion fully, i.e., to detect and analyze all wave modes and both propagating and evanescent waves in all regions of the device. The laser interferometric technique presented here detects the out-of-plane surface vibration component, and through this measurement, is able to characterize the lateral component of the wave vector. The technique is based on electrical excitation of the sample, and therefore, the detection of the vibrations outside of the active regions relies on wave content due to the excitation of the active structure. The evanescent wave modes and measuring their dispersion are fundamentally different from the conventional dispersion measurement of propagative wave modes in the sense that they represent non-propagating waves that do not transport energy.

While several authors have utilized the possibility to calculate BAW dispersion diagrams from laser interferometric wave field measurements from the active resonator area, Publication VI is the first to extend this capability to the sourceless regions as well. The remaining challenge is to be able to characterize also the evanescent waves. Publication VII demonstrates the extension of the analysis of the measurement data to allow also for the extraction of the dispersion diagram of the imaginary wave vectors for the outside region.
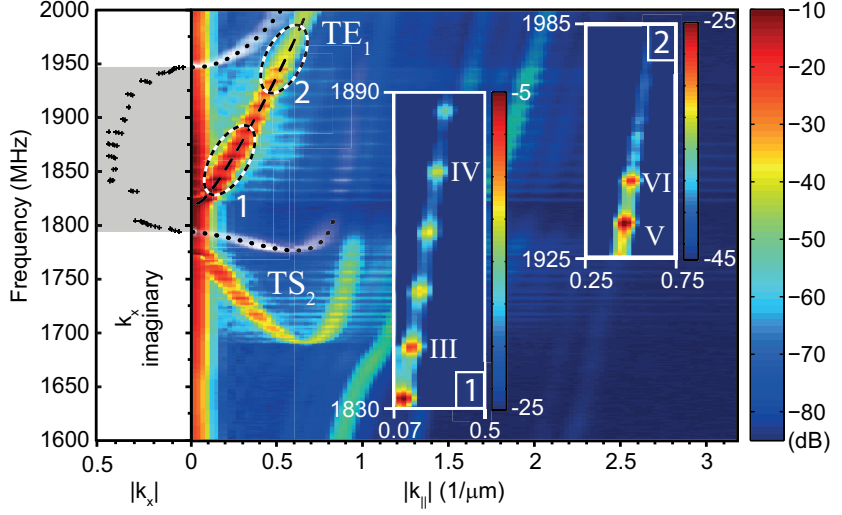
Figure 5.9. Dispersion diagram for both resonator and outside regions calculated from the measured wave field data from the 1820 MHz AlN thin film BAW resonator. The dispersion diagram from the active area of the resonator is plotted with colors ranging from deep blue to red, while the dispersion diagram obtained from the outside area is superposed using shades of gray, and the mode branches of the outside dispersion are indicated with a dotted line to guide the eye. Furthermore, the outside regions' evanescent branch, obtained via a function fit to the amplitude line data, is provided on the left hand side as crosses. Due to the finite lateral dimensions of the sample and high-Q resonances, the TE_1 dispersion curve (marked with dashed line) is seen in the dispersion diagram as a chain of discrete maxima. Parts of the TE_1 curve, the beginning and just before and after the upper cut-off frequency of the lateral energy trapping frequency range, are further enlarged and provided as insets (1 and 2) to enable better visualization of the eigenresonances and the behavior near the cutoff, where they vanish. The two last eigenresonances, 1933 MHz and 1944 MHz, are marked with V and VI, respectively, and correspond to the resonance peaks in Fig. 5.10(a). The corresponding amplitude distributions are presented in Fig. 5.7.

In contrast to calculating the dispersion diagram for propagating waves, utilizing Fourier transform, the imaginary wave-vectors are determined from the wave field images by detecting the exponentially decaying wave amplitude characteristic to an evanescent wave. To extract a numerical value, an exponential function is fitted to the amplitude line profile, thereby yielding the characteristic decay length. Three examples of the extracted amplitude line profiles and of the function fits are provided in Fig. 5.10(b). Plotting the magnitudes of the obtained imaginary wave vectors at a range of frequencies provides a good indication of the shape and magnitude of the imaginary branch in the dispersion diagram, see the left-hand-side in Fig. 5.9.
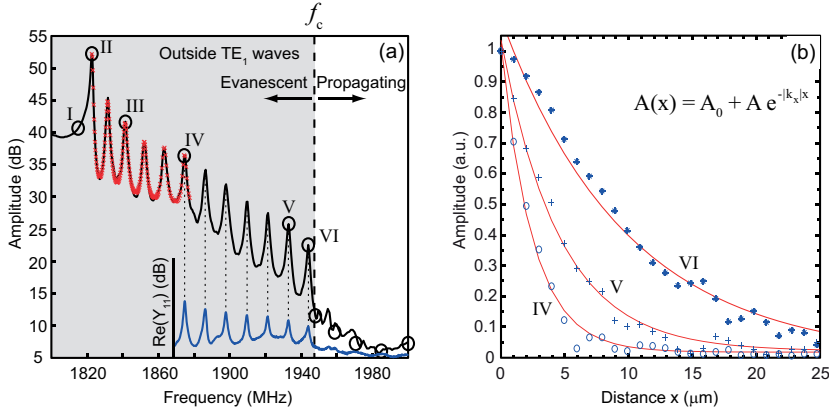
Figure 5.10. (a) Extracted vibration amplitude (in logarithmic scale) along the TE_1 mode branch as a function of frequency. The result of fitting the mechanical equivalent circuit (mBvD) model to the 6 first eigenresonances of the data is shown with red crosses (x). A zoomed view on the real part of admittance $[Re(Y_{11})]$, measured electrically on wafer, is provided as an inset (blue curve). The spurious electrical resonances are observed to correspond to the eigenresonances of the TE_1 mode and both vanish abruptly at around $f_c \sim 1947$ MHz. The gray shading denotes the lateral energy trapping frequency range of the resonator determined via the dispersion measurements. (b) Three examples of the extracted amplitude line profiles and the exponential function fits used to extract the imaginary part of the outside dispersion.

The ability to experimentally characterize the evanescent part of the wave dispersion is a significant advancement of laser interferometric data-analysis for extracting dispersion properties. This could prove especially useful in the research and development of laterally coupled BAW resonator filters [141, 147, 148], where the coupling between the resonators is accomplished via evanescent waves.

6.   Conclusion

The research work summarized in this thesis comprises the design, implementation and characterization of a state-of-the-art heterodyne laser interferometer as well as the development and application of interferometer data-analysis techniques to microacoustic devices and test structures. The need for high-quality, phase-sensitive, absolute-amplitude data is the binding element between all the publications, which report either characterization of device physics in novel microacoustic devices, or new and advanced data-analysis techniques.

Publication I provides a detailed description and performance characterization of the heterodyne laser interferometer. The interferometer combines many of the desired characteristics of a high-performance research instrument, such as simultaneous acquisition of amplitude and phase of the vibration, high sensitivity with minimum detectable amplitudes of even less than 1 pm, and a lateral resolution better than 1 μm. The heterodyne concept offers immunity against RF-leakage from sample excitation to the signal detection, due to the frequency offset between the two. The photodetector and the detection electronics provide a flat frequency response, up to 6 GHz, enabling quantitative analysis over a wide frequency range. The setup utilizes a frequency sweep at each measurement point, resulting in high measurement speed.

Publication II is among the first to investigate the actual vibration fields in a phononic crystal structure. The laser interferometer is utilized to characterize the interaction of SAWs with the phononic crystal structure in detail. The measurements not only provided a direct experimental confirmation of the existence of the theoretically predicted bandgap for the SAWs but also revealed a reason for an unexpected loss of electrical signal above the bandgap frequency range. The measurements also show the

ability of the interferometer to extract vibration data even from within the phononic crystal structure, where the high filling fraction results in only small crystal areas between the etched holes.

Publication III presents a novel method for extracting the materials parameters of a substrate by interferometric measurement of a random wave field. The experiment also serves to demonstrate the interferometer's ability to acquire high-quality phase-sensitive data with a small minimum detectable amplitude of the surface vibrations. A small minimum detectable amplitude enables the characterization of weak effects, such as scattered SAW fields in a sourceless region. Use of Fourier transform methods to further analyze the observed weak random-looking SAW field reveals the slowness curve for the SAWs without any prior knowledge of the wave propagation. Furthermore, the result shows that, rather surprisingly, the random scattering structures scatter the incoming directional SAW beams also significantly to BAWs with a fairly uniform distribution of $k_\parallel$ values.

Publications IV-VII all push the state-of-the-art of laser interferometric measurement of plate wave dispersion and promote the further use of the dispersion data. Publication IV demonstrates the extraction of mirror transfer characteristics from high-quality measurement data obtained from the top of the resonator and from the bottom of the mirror, providing a first direct experimental measurement to quantify the amount of longitudinal waves leaking through the mirror. A sensitive setup is needed to be able to compare the measured wave fields on the top and at the bottom, since the backside wave field is very weak. In addition to the comparison of the measured wave fields, dispersion diagrams were calculated from both data sets and utilized to quantify the frequency dependent mirror transfer function for longitudinal waves, a result that can be directly compared with the simulations. The results confirm the validity of the commonly used 1D simulations for modeling the longitudinal wave behavior in the thin film layer stack.

Already in our research of the transfer function of the acoustic mirror, the close inspection of the detailed dispersion data showed that the TE_1 mode branch is actually a chain of maxima, where the maxima are caused by the lateral standing wave resonances arising in the resonator structure. The observed mechanical behavior was correlated with spurious resonances in the electrical response, and reported in our early re-

sults [85,142]. This is the first experimental result to show the connection between the two, and has been credited to verify the theoretical reasoning that the lateral standing wave resonances in the structure are responsible for the electrical spurious responses [132]. In Publication V the phenomenon is studied with another sample having a different geometry, resonance frequency and piezoelectric material. The data analysis is advanced further to isolate the response of a single mode branch and to extract information on the individual lateral eigenresonances arising in the BAW resonator. A function fit to the resulting frequency response data of the TE_1 eigenresonances is utilized to extract detailed information about the individual eigenresonances. An excellent match between the fit and the data indicates the validity of the mBvD model, often used to describe the electrical behavior of a multi-mode resonator.

Publications VI and VII further advance the dispersion data analysis techniques to enable the extraction of plate wave dispersion properties of the source-less, outside, region of a resonator. The articles are the first to develop and demonstrate the capability to experimentally quantify the dispersion properties of both propagating and evanescent waves in the outside region. These results serve, yet again, to verify the theoretical understanding of the resonator physics. Together with the data from the active area, and from electrical measurements, the wave behavior in the resonator can be correlated with the electrical response to experimentally determine the lateral energy trapping range, and to show that the sudden disappearance of the electrical spurious responses is a result of exceeding the upper cutoff frequency. This is consistent with our previous results, providing further proof that the spurious electrical responses are due to lateral eigenresonances in the resonator structure. The ability to measure the outside dispersion properties provides a unique experimental view on the resonator physics and is expected to especially benefit the development of more complex devices, such as laterally acoustically coupled resonator filters.

The work described in this thesis has advanced both the performance of the optical measurement setup and the use of the interferometric measurement data in the field of characterization and analysis of surface vibrations in microacoustic components. A possible direction to proceed in the future would be to extend the capabilities of the interferometric measurement technique towards characterization and analysis of nonlinear

vibrations and effects. As the required performance level of the electroa-
coustic devices rises, nonlinearity issues arise even in components tradi-
tionally considered linear, such as SAW resonators and filters. Especially
SAW and BAW filter research and development is likely to benefit from a
direct experimental characterization of mechanical nonlinear effects. The
challenge for the measurement technology is the inherent nonlinearity of
the interferometric detection and the consequent need to separate the ac-
tual nonlinear mechanical effects from the nonlinear signal produced by
the detection method.

The increasing demands on the performance of SAW and BAW based
components, intense research effort devoted to the phononic crystals, and
the ongoing development of micromechanical components, call for versa-
tile metrology solutions for characterization of the vibration fields in a
variety of electroacoustic components. Together with the need to further
advance the understanding of the physics of wave behavior in complex mi-
croacoustic structures and acoustic metamaterials, this makes advanced
optical measurement methods an attractive topic for future research.

Bibliography

[1] Rayleigh, L. On waves propagating along the plane surface of an elastic solid. In *Proc. London Math. Soc.*, vol. 7, 4–11 (1885).

[2] Curie, J. & Curie, P. Développement par pression, de l'électricité polaire dans les cristaux hémièdres à faces inclinées. In *Comptes Rendus*, vol. 91, 294 (1880).

[3] White, R. M. & Voltmer, F. W. Direct piezoelectric coupling to surface elastic waves. *Appl. Phys. Lett.* **17**, 314–316 (1965).

[4] Maiman, T. H. Stimulated optical radiation in ruby. *Nature* **187**, 493–494 (1960).

[5] Lean, E. G. H. & Powell, C. G. Optical probing of surface acoustic waves. In *Proc. of the IEEE*, vol. 58, 1939–1947 (1970).

[6] Lean, E. G. *Progress in optics*, vol. XI, chap. Interaction of light and acoustic surface waves, 124–166 (North-Holland publishing company, 1973).

[7] Cambon, G., Rouzeyre, M. & Simon, G. Optical probing of surface rayleigh waves. *Applied Physics Letters* **18**, 295–298 (1971).

[8] Adler, R., Korpel, A. & Desmares, P. An instrument for making surface waves visible. *IEEE Trans. SU* **SU-15**, 157–161 (1968).

[9] Slobodnik, Jr., A. J. Microwave frequency acoustic surface wave propagation losses in $LiNbO_3$. *Applied Physics Letters* **14**, 94–96 (1969).

[10] Slobodnik, Jr., A. J., Carr, P. H. & Budreau, A. J. Microwave frequency acoustic surface-wave loss mechanisms on $LiNbO_3$. *J. Appl. Phys.* **41**, 4380–4387 (1970).

[11] Engan, H. E. Phase sensitive laser probe for high-frequency surface acoustic wave measurements. *IEEE Trans. SU* **SU-25**, 372–377 (1978).

[12] Anhorn, M., Engan, H. & Ronnekleiv, A. New SAW velocity measurements on Y-cut $LiNbO_3$. In *IEEE 1987 Ultrasonics Symposium*, 279–284 (1987).

[13] Ginter, A. & Sölkner, G. Phase accurate optical probing of surface acoustic wave devices. *Applied Physics Letters* **56**, 2295–2297 (1990). URL http://link.aip.org/link/?APL/56/2295/1.

[14] Kovacs, G., Anhorn, M., Engan, H. E., Visintini, G. & Ruppel, C. C. W. Improved material constants for $LiNbO_3$ and $LiTaO_3$. In *Proc. IEEE Ultrasonics Symposium*, 435–438 (1990).

[15] Jen, S. & Domalewski, M. Techniques for SAW device investigation using a high-performance phase-sensitive laser probe. In *Ultrasonics Symposium, 1992. Proceedings., IEEE 1992*, 433–436 (1992).

[16] Engan, H. E. & Ronnekleiv, A. Enhancement of SAW laser probe measurements by signal processing. In *Proc. IEEE Ultrasonics Symposium*, 217–220 (1999).

[17] Kamizuma, H., Yang, L., Omori, T., ya Hashimoto, K. & Yamaguchi, M. High-speed laser probing system for surface acoustic wave devices based on knife-edge method. *Japanese Journal of Applied Physics* **44**, 4535–4538 (2005).

[18] Kamizuma, H., Omori, T., Hamishoto, K. & Yamaguchi, M. Development of fast-scanning laser probe system based on knife-edge method for diagnosis of RF surface acoustic wave devices. *Ultrasonics, Ferroelectrics and Frequency Control, IEEE Transactions on* **53**, 1186–1191 (2006).

[19] Hashimoto, K., Kamizuma, H., Watanabe, M., Omori, T. & Yamaguchi, M. Wavenumber domain analysis of two-dimensional SAW images captured by phase-sensitive laser probe system. In *Proc. IEEE Ultrason. Symp.*, 367–370 (2006).

[20] Hashimoto, K., Kamizuma, H., Watanabe, M., Omori, T. & Yamaguchi, M. Wavenumber domain analysis of two-dimensional SAW images captured by phase-sensitive laser probe system. *IEEE Trans. Ultrason., Ferroelect., Freq. Contr.* **54**, 1072–1075 (2007).

[21] Whitman, R. L., Laub, L. J. & Bates, W. J. Acoustic surface displacement measurements on a wedge-shaped transducer using an optical probe technique. *IEEE Trans. SU* **SU-15**, 186–189 (1968).

[22] Whitman, R. L. & Korpel, A. Probing of acoustic surface perturbations by coherent light. *Appl. Opt.* **8**, 1567–1576 (1969).

[23] Monchalin, J. P. Heterodyne interferometric laser probe to measure continuous ultrasonic displacements. *Rev. Sci. Instrum.* **56**, 543–546 (1985).

[24] Royer, D. & Dieulesaint, E. Optical probing of the mechanical impulse response of a transducer. *Appl. Phys. Lett.* **49**, 1056–1058 (1986).

[25] Gindre, M., Urbach, W., Coursant, R. H. & Fink, M. Mechanical displacement induced in a piezoelectric structure: Experimental measurement by laser interferometry and simulation by a finite element method. *J. Acoust. Soc. Amer.* **84**, 11–19 (1988).

[26] Pouet, B. F., Ing, R. K., Krishnaswamy, S. & Royer, D. Heterodyne interferometer with two-wave mixing in photorefractive crystals for ultrasound detection on rough surfaces. *Applied Physics Letters* **69**, 3782–3784 (1996).

[27] Knuuttila, J. V., Tikka, P. T. & Salomaa, M. M. Scanning Michelson interferometer for imaging surface acoustic wave fields. *Opt. Lett.* **25**, 613–615 (2000).

[28] Fattinger, G. G. & Tikka, P. T. Modified Mach-Zehnder laser interferometer for probing bulk acoustic waves. *Appl. Phys. Lett.* **79**, 290–292 (2001).

[29] Telschow, K. L., Deason, V. A., Cottle, D. L. & J. D. Larson, I. Full-field imaging of gigahertz film bulk acoustic resonator motion. *IEEE Trans. Ultrason., Ferroelect., Freq. Contr.* **50**, 1279–1285 (2003).

[30] Chiba, T. Optical proving of acoustic field distribution within surface acoustic wave devices by heterodyne interferometry. *IEICE Trans.* **J86-C**, 1302–1308 (2003). In Japanese.

[31] Martinussen, H., Aksnes, A. & Engan, H. E. Wide frequency range measurements of absolute phase and amplitude of vibrations in micro- and nanostructures by optical interferometry. *Opt. Express* **15**, 11370–11384 (2007).

[32] Hashimoto, K. *et al.* A laser probe based on a sagnac interferometer with fast mechanical scan for RF surface and bulk acoustic wave devices. *Ultrasonics, Ferroelectrics and Frequency Control, IEEE Transactions on* **58**, 187–194 (2011).

[33] Leirset, E., Engan, H. E. & Aksnes, A. Heterodyne interferometer for absolute amplitude vibration measurements with femtometer sensitivity. *Opt. Express* **21**, 19900–19921 (2013). URL http://www.opticsexpress.org/abstract.cfm?URI=oe-21-17-19900.

[34] Knuuttila, J. *Laser-Interferometric Analysis of Surface Acoustic Wave Resonators*. Ph.D. thesis, Materials Physics Laboratory, Helsinki University of Technology, Espoo (2005).

[35] Schmidt, R. V. Optical probing of bulk waves present in acoustic surface wave delay lines. *Applied Physics Letters* **17**, 369–371 (1970).

[36] Jia, X., Boumiz, A. & Quentin, G. Laser interferometric detection of ultrasonic waves propagating inside a transparent solid. *Applied Physics Letters* **63**, 2192–2194 (1993).

[37] Miyamoto, A., Wakana, S. & Ito, A. Novel optical observation technique for shear horizontal wave in SAW resonators on $42°$YX-cut lithium tantalate. In *Proc. IEEE Ultrasonics Symposium*, 89–92 (2002).

[38] Wakana, S., Miyamoto, A. & Ito, A. Backside observation technique for SAW distribution under electrodes. In *Proc. IEEE Ultrasonics Symposium*, 1714–1717 (2003).

[39] Matsuda, S., Miyamoto, A., Wakana, S. & Ito, A. Observation of waves propagating within a substrate. In *Ultrasonics Symposium, 2004 IEEE*, 1876–1879 (2004).

[40] Watanabe, Y., Gola, S., Sato, T. & Sekimoto, H. Nonscanning measurements for determining in-plane mode shapes in piezoelectric devices with polished surfaces. *IEEE Trans. Ultrason., Ferroelect., Freq. Contr.* **51**, 491–495 (2004).

[41] Shajenko, P. & Johnson, C. D. Stroboscopic holographic interferometry. *Applied Physics Letters* **13**, 44–46 (1968).

[42] Archbold, E. & Ennos, A. E. Observation of surface vibration modes by stroboscopic hologram interferometry. *Nature* **217**, 942–943 (1968).

[43] Kamshilin, A. A., Romashko, R. V. & Kulchin, Y. N. Adaptive interferometry with photorefractive crystals. *Journal of Applied Physics* **105**, 031101 (2009). URL http://link.aip.org/link/?JAP/105/031101/1.

[44] Hesjedal, T., Chilla, E. & Fröhlich, H. J. High resolution visualization of acoustic wave fields within surface acoustic wave devices. *Appl. Phys. Lett.* **70**, 1372–1374 (1997).

[45] Safar, H. *et al.* Imaging of acoustic fields in bulk acoustic-wave thin-film resonators. *Appl. Phys. Lett.* **77**, 136–138 (2000).

[46] Hesjedal, T. & Behme, G. High-resolution imaging of a single circular surface acoustic wave source: Effects of crystal anisotropy. *Appl. Phys. Lett.* **79**, 1054–1056 (2001).

[47] Paulo, A. S., Liu, X. & Bokor, J. Scanning acoustic force microscopy characterization of thermal expansion effects on the electromechanical properties of film bulk acoustic resonators. *Applied Physics Letters* **86**, 084102 (2005).

[48] Ryder, S., Lee, K. B., Meng, X. & Lin, L. AFM characterization of out-of-plane high frequency microresonators. *Sens. Actuators A* **114**, 135–140 (2004).

[49] Paulo, A. S., Black, J. P., White, R. M. & Bokor, J. Detection of nanomechanical vibrations by dynamic force microscopy in higher cantilever eigenmodes. *Applied Physics Letters* **91**, 053116 (2007).

[50] Eberharter, G. & Feuerbaum, H. Scanning-electron-microscope observations of propagating acoustic waves in surface acoustic wave devices. *Applied Physics Letters* **37**, 698–699 (1980).

[51] Zolotoyabko, E., Shilo, D., Sauer, W., Pernot, E. & Baruchel, J. Visualization of 10 μm surface acoustic waves by stroboscopic x-ray topography. *Applied Physics Letters* **73**, 2278–2280 (1998).

[52] Tucoulou, R. *et al.* Electromigration in Al thin films induced by surface acoustic waves: application to imaging. *Ultrasonics, Ferroelectrics and Frequency Control, IEEE Transactions on* **46**, 856–860 (1999).

[53] Tan, M. K., Friend, J. R. & Yeo, L. Y. Direct visualization of surface acoustic waves along substrates using smoke particles. *Applied Physics Letters* **91**, 224101 (2007).

[54] Grahn, H., Maris, H. & Tauc, J. Picosecond ultrasonics. *Quantum Electronics, IEEE Journal of* **25**, 2562–2569 (1989).

[55] Wright, O. B. & Kawashima, K. Coherent phonon detection from ultrafast surface vibrations. *Phys. Rev. Lett.* **69**, 1668–1671 (1992).

[56] Wright, O. B. & Gusev, V. E. Acoustic generation in crystalline silicon with femtosecond optical pulses. *Applied Physics Letters* **66**, 1190–1192 (1995).

[57] Hurley, D. H. & Telschow, K. L. Simultaneous microscopic imaging of elastic and thermal anisotropy. *Phys. Rev. B* **71**, 241410 (2005).

[58] Zhang, S., Péronne, E., Belliard, L., Vincent, S. & Perrin, B. Three-dimensional acoustic wavefront imaging in anisotropic systems by picosecond acoustics. *Journal of Applied Physics* **109**, 033507 (2011).

[59] Devos, A., Robillard, J.-F., Côte, R. & Emery, P. High-laser-wavelength sensitivity of the picosecond ultrasonic response in transparent thin films. *Phys. Rev. B* **74**, 064114 (2006).

[60] Sugawara, Y. *et al.* Watching ripples on crystals. *Phys. Rev. Lett.* **88**, 185504 (2002).

[61] Tachizaki, T. *et al.* Scanning ultrafast sagnac interferometry for imaging two-dimensional surface wave propagation. *Rev. Sci. Instrum.* **77**, 043713 (2006).

[62] Dhar, L. & Rogers, J. A. High frequency one-dimensional phononic crystal characterized with a picosecond transient grating photoacoustic technique. *Applied Physics Letters* **77**, 1402–1404 (2000).

[63] Profunser, D. M., Wright, O. B. & Matsuda, O. Imaging ripples on phononic crystals reveals acoustic band structure and bloch harmonics. *Phys. Rev. Lett.* **97**, 055502 (2006).

[64] Danworaphong, S. *et al.* Real-time imaging of acoustic rectification. *Applied Physics Letters* **99**, 201910 (2011).

[65] Maznev, A. A., Wright, O. B. & Matsuda, O. Mapping the band structure of a surface phononic crystal. *New Journal of Physics* **13**, 013037 (2011).

[66] de la Rue, R., Humphryes, R., Mason, I. & Ash, E. Acoustic-surface-wave amplitude and phase measurements using laser probes. *Electrical Engineers, Proceedings of the Institution of* **119**, 117–126 (1972).

[67] Stegeman, G. I. Optical probing of surface waves and surface wave devices. *IEEE Trans. SU* **SU-23**, 33–63 (1976).

[68] Monchalin, J. P. Optical detection of ultrasound. *IEEE Trans. Ultrason., Ferroelect., Freq. Contr.* **33**, 485–499 (1986).

[69] Donati, S. *Electro-optical instrumentation: sensing and measuring with lasers* (Prentice Hall, 2004).

[70] Karasik, A. Y., Rinkevichius, B. S. & Zubov, V. A. *Laser interferometry principles* (Mir Publishers, 1995).

[71] Lauterborn, W., Kurz, T. & Wiesenfeldt, M. *Coherent optics: Fundamentals and applications* (Springer, 1995).

[72] Hariharan, P. *Basics of interferometry* (Academic Press, 1992).

[73] Scruby, C. B. & Drain, L. E. *Laser ultrasonics: Techniques and applications* (Adam Hilger, 1990).

[74] Royer, D. & Dieulesaint, E. *Elastic Waves in Solids II* (Springer-Verlag, Berlin, 2000).

[75] Wolfe, J. P. *Imaging phonons: acoustic wave propagation in solids* (Cambridge university press, 1998).

[76] Wagner, J. W. Optical detection of ultrasound. *Physical Acoustics* **XIX** (1990).

[77] Fattinger, G. & Marksteiner, S. *RF bulk acoustic wave filters for communications*, chap. Characterization of BAW devices, 201–204 (Artech House, 2009).

[78] Dransfeld, K. & Salzmann, E. *Physical Acoustics*, vol. VII, chap. 4, 242–250 (Academic Press, 1970).

[79] Knuuttila, J. *Advanced Interferometric Imaging System for Surface Acoustic Waves*. Master's thesis, Materials Physics Laboratory, Helsinki University of Technology, Espoo (1998).

[80] Kokkonen, K. *Design and characterization of a heterodyne laser interferometer*. Master's thesis, Materials Physics Laboratory, Helsinki University of Technology, Espoo (2005).

[81] Holmgren, O. *Laser-Probe Analysis of Modern Electroacoustic Microwave Devices*. Ph.D. thesis, Department of Applied Physics, Helsinki University of Technology, Espoo (2009).

[82] Lipiäinen, L., Kokkonen, K. & Kaivola, M. Phase sensitive absolute amplitude detection of surface vibrations using homodyne interferometry without active stabilization. *J. Appl. Phys.* **108**, 114510 (2010).

[83] Graebner, J. E. Optical scanning interferometer for dynamic imaging of high-frequency surface motion. In *Proc. IEEE Ultrasonics Symposium*, vol. 1, 733–736 (2000).

[84] Wagner, J. W. & Spicer, J. B. Theoretical noise-limited sensitivity of classical interferometry. *J. Opt. Soc. Am. B* **4**, 1316–1326 (1987).

[85] Kokkonen, K., Pensala, T. & Kaivola, M. Interferometric measurements of dispersion curves and transmission characteristics of the acoustic mirror in thin film BAW resonator. In *Proc. IEEE MTT-S Int. Microwave Symp.*, 2071–2074 (2007).

[86] Kokkonen, K. Laser interferometers in physical acoustics. In *Ultrasonics Symposium (IUS), 2009 IEEE International*, 1036–1043 (2009).

[87] Hays, R. & Hartmann, C. Surface-acoustic-wave devices for communications. *Proceedings of the IEEE* **64**, 652–671 (1976).

[88] Ruppel, C. *et al.* SAW devices for consumer communication applications. *Ultrasonics, Ferroelectrics and Frequency Control, IEEE Transactions on* **40**, 438–452 (1993).

[89] Pohl, A. A review of wireless SAW sensors. *Ultrasonics, Ferroelectrics and Frequency Control, IEEE Transactions on* **47**, 317–332 (2000).

[90] Ballantine, D. S. *et al. Acoustic Wave Sensors* (Academic Press, 1997).

[91] Thompson, M. & Stone, D. C. *Surface-Launched Acoustic Wave Sensors* (John Wiley & Sons, 1997).

[92] Selmeier, P. *et al.* Recent advances in SAW packaging. In *Ultrasonics Symposium, 2001 IEEE*, 283–292 (2001).

[93] Bhattacharjee, K., Shvetsov, A. & Zhgoon, S. Cavityless wafer level packaging of SAW devices. In *Ultrasonics Symposium, 2007. IEEE*, 1886–1889 (2007).

[94] Hashimoto, K.-y. *et al.* Piezoelectric boundary acoustic waves: Their underlying physics and applications. In *Ultrasonics Symposium, 2008. IUS 2008. IEEE*, 999–1005 (2008).

[95] Kushwaha, M. S., Halevi, P., Dobrzynski, L. & Djafari-Rouhani, B. Acoustic band structure of periodic elastic composites. *Phys. Rev. Lett.* **71**, 2022–2025 (1993).

[96] Sigalas, M. & Economou, E. Band structure of elastic waves in two dimensional systems. *Solid State Communications* **86**, 141–143 (1993).

[97] Olsson, R. H. & El-Kady, I. Microfabricated phononic crystal devices and applications. *Measurement Science and Technology* **20**, 012002 (13pp) (2009).

[98] Pennec, Y., Vasseur, J. O., Djafari-Rouhani, B., Dobrzynski, L. & Deymier, P. A. Two-dimensional phononic crystals: Examples and applications. *Surface Science Reports* **65**, 229–291 (2010).

[99] Khelif, A. *et al.* The omnisaw device concept (omnisaw: Omnidirectional band gap for surface acoustic wave). In *Ultrasonics Symposium, 2008. IUS 2008. IEEE*, 304–307 (2008).

[100] Auld, B. A. *Acoustic Fields and Waves in Solids*, vol. 1 (Robert E. Krieger Publishing Company, 1990), 2 edn.

[101] Auld, B. A. *Acoustic Fields and Waves in Solids*, vol. 2 (Robert E. Krieger Publishing Company, 1990), 2 edn.

[102] Hashimoto, K. *Surface Acoustic Wave Devices in Telecommunications* (Springer-Verlag, Berlin, 2000).

[103] Morgan, D. P. *Surface-Wave Devices for Signal Processing* (Elsevier, Amsterdam, 1991).

[104] Campbell, C. *Surface Acoustic Wave Devices and Their Signal Processing Applications* (Academic Press, San Diego, 1989).

[105] Makkonen, T. *et al.* FEM/BEM simulation and experimental study of LL-SAW resonator characteristics on YZ-LiNbO$_3$. In *Proc. IEEE Ultrasonics Symposium*, 305–308 (2002).

[106] Solal, M. *et al.* FEM/BEM analysis for SAW devices. In *Second International Symposium on Acoustic Wave Devices for Future Mobile Communication Systems*, 185–202 (2004).

[107] Solal, M., Chen, L. & Gratier, J. Measurement and FEM/BEM simulation of transverse effects in SAW resonators in lithium tantalate. In *Ultrasonics Symposium (IUS), 2010 IEEE*, 175–180 (2010).

[108] Knuuttila, J. V., Tikka, P. T., Hartmann, C. S., Plessky, V. P. & Salomaa, M. M. Anomalous asymmetric acoustic radiation in low-loss SAW filters. *Electron. Lett.* **35**, 1115–1116 (1999).

[109] Koskela, J. *et al.* Mechanism for acoustic leakage in surface-acoustic wave resonators on rotated Y-cut lithium tantalate substrate. *Appl. Phys. Lett.* **75**, 2683–2685 (1999).

[110] Koskela, J., Knuuttila, J. V., Makkonen, T., Plessky, V. P. & Salomaa, M. M. Acoustic loss mechanisms in leaky SAW resonators on lithium tantalate. *IEEE Trans. Ultrason., Ferroelect., Freq. Contr.* **48**, 1517–1526 (2001).

[111] Benchabane, S., Khelif, A., Rauch, J.-Y., Robert, L. & Laude, V. Evidence for complete surface wave band gap in a piezoelectric phononic crystal. *Phys. Rev. E* **73**, 065601(R) (2006).

[112] Aono, T. & Tamura, S.-i. Surface and pseudosurface acoustic waves in superlattices. *Phys. Rev. B* **58**, 4838–4845 (1998).

[113] Tanaka, Y. & Tamura, S.-i. Acoustic stop bands of surface and bulk modes in two-dimensional phononic lattices consisting of aluminum and a polymer. *Phys. Rev. B* **60**, 13294–13297 (1999).

[114] Torres, M., Montero de Espinosa, F. R., García-Pablos, D. & García, N. Sonic band gaps in finite elastic media: Surface states and localization phenomena in linear and point defects. *Phys. Rev. Lett.* **82**, 3054–3057 (1999).

[115] Wu, T.-T., Huang, Z.-G. & Lin, S. Surface and bulk acoustic waves in two-dimensional phononic crystal consisting of materials with general anisotropy. *Phys. Rev. B* **69**, 094301 (2004).

[116] Laude, V., Wilm, M., Benchabane, S. & Khelif, A. Full band gap for surface acoustic waves in a piezoelectric phononic crystal. *Phys. Rev. E* **71**, 036607 (2005).

[117] Wu, T.-T., Wu, L.-C. & Huang, Z.-G. Frequency band-gap measurement of two-dimensional air/silicon phononic crystals using layered slanted finger interdigital transducers. *Journal of Applied Physics* **97**, 094916 (2005).

[118] Benchabane, S., Robert, L., Rauch, J.-Y., Khelif, A. & Laude, V. Highly selective electroplated nickel mask for lithium niobate dry etching. *Journal of Applied Physics* **105**, 094109 (2009).

[119] Wickramasinghe, H. & Ash, E. Surface acoustic wave slowness surface measurement. In *1975 Ultrasonics Symposium*, 496–498 (1975).

[120] Robbins, W. P. & Rudd, E. P. Measurement of surface acoustic wave slowness curves with a scanning laser acoustic microscope. *J. Appl. Phys.* **64**, 1040–1043 (1988).

[121] Laude, V. *et al.* Subwavelength focusing of surface acoustic waves generated by an annular interdigital transducer. *Appl. Phys. Lett.* **92**, 094104 (2008).

[122] Day, C. & Koerber, G. Annular piezoelectric surface waves. *Sonics and Ultrasonics, IEEE Transactions on* **19**, 461–465 (1972).

[123] Laude, V., Jerez-Hanckes, C. & Ballandras, S. Surface Green's function of a piezoelectric half-space. *Ultrasonics, Ferroelectrics and Frequency Control, IEEE Transactions on* **53**, 420–428 (2006).

[124] Laude, V., Kokkonen, K., Benchabane, S. & Kaivola, M. Material anisotropy unveiled by random scattering of surface acoustic waves. *Appl. Phys. Lett.* **98**, 063506 (2011).

[125] Nuttall, A. Some windows with very good sidelobe behavior. *Acoustics, Speech and Signal Processing, IEEE Transactions on* **29**, 84–91 (1981).

[126] Cady, W. G. The piezo-electric resonator. *Proc. I.R.E.* **10**, 83–114 (1922).

[127] Gerber, E. & Sykes, R. Quartz frequency standards. *Proceedings of the IEEE* **55**, 783–791 (1967).

[128] Lombardi, M. The evolution of time measurement, part 2: quartz clocks [recalibration]. *Instrumentation Measurement Magazine, IEEE* **14**, 41–48 (2011).

[129] Lam, C. A review of the recent development of mems and crystal oscillators and their impacts on the frequency control products industry. In *Ultrasonics Symposium, 2008. IUS 2008. IEEE*, 694–704 (2008).

[130] Newell, W. E. Face-mounted piezoelectric resonators. *Proc. IEEE* **53**, 575–581 (1965).

[131] Aigner, R. Bringing BAW technology into volume production: The ten commandments and the seven deadly sins. In *3rd International Symposium on Acoustic Wave Devices for Future Mobile Communication Systems* (2007).

[132] Kaitila, J. *RF bulk acoustic wave filters for communications*, chap. BAW Device Basics, 51–90 (Artech House, 2009).

[133] Thalhammer, R. & Aigner, R. Energy loss mechanisms in smr-type baw devices. In *Microwave Symposium Digest, 2005 IEEE MTT-S International*, 225–228 (2005).

[134] Ruby, R. *et al.* Positioning FBAR technology in the frequency and timing domain. *Ultrasonics, Ferroelectrics and Frequency Control, IEEE Transactions on* **59**, 334–345 (2012).

[135] Lowe, M. J. Matrix techniques for modeling ultrasonic waves in multilayered media. *IEEE Trans. Ultrason., Ferroelect., Freq. Contr.* **42**, 525–542 (1995).

[136] Marksteiner, S., Kaitila, J., Fattinger, G. & Aigner, R. Optimization of acoustic mirrors for solidly mounted baw resonators. In *Ultrasonics Symposium, 2005 IEEE*, vol. 1, 329 – 332 (2005).

[137] Pensala, T. *Thin Film Bulk Acoustic Wave Devices*. Ph.D. thesis, Department of Applied Physics, Aalto University, Espoo (2011).

[138] Pensala, T., Thalhammer, R., Dekker, J. & Kaitila, J. Experimental investigation of acoustic substrate losses in 1850-MHz thin film BAW resonators. *Ultrasonics, Ferroelectrics and Frequency Control, IEEE Transactions on* **56**, 2544–2552 (2009).

[139] Kaitila, J., Ylilammi, M., Ellä, J. & Aigner, R. Spurious resonance free bulk acoustic wave resonators. In *Proc. IEEE Ultrasonics Symposium*, 84–87 (2003).

[140] Rosén, D., Bjurström, J. & Katardjiev, I. Suppression of spurious lateral modes in thickness-excited FBAR resonators. *IEEE Trans. on Ultrasonics, Ferroelectrics, and Frequency Control* **52**, 1189–1192 (2005).

[141] Meltaus, J., Pensala, T. & Kokkonen, K. Modelling of 2-D lateral modes in solidly-mounted BAW resonators. In *Ultrasonics Symposium, 2008. IUS 2008. IEEE*, 1544–1547 (2008).

[142] Kokkonen, K. & Pensala, T. Laser interferometric measurements and simulations of waves transmitted through the acoustic mirror in thin film BAW resonator. In *Proc. IEEE Ultrasonics Symposium*, 460–463 (2006).

[143] Strijbos, R., Jansman, A., Lobeek, J.-W., Li, N. & Pulsford, N. Design and characterisation of high-Q solidly-mounted bulk acoustic wave filters. In *Electronic Components and Technology Conference, 2007. ECTC '07. Proceedings. 57th*, 169–174 (2007).

[144] Auld, B. A. *Acoustic Fields and Waves in Solids*, vol. 2, 260–261 (Robert E. Krieger Publishing Company, 1990), 2 edn.

[145] Wu, N., Hashimoto, K., Kashiwa, K., Omori, T. & Yamaguchi, M. Study on the frequency dependence of lateral energy leakage in RF bulk acoustic wave device by fast-scanning laser probe system. *Japanese Journal of Applied Physics* **48**, 07GG01 (2009).

[146] Thalmayr, F., Hashimoto, K., Ueda, M., Omori, T. & Yamaguchi, M. Quantitative analysis of power leakage in an film bulk acoustic resonator device at the antiresonance frequency. *Japanese Journal of Applied Physics* **49**, 07HD11 (2010).

[147] Meltaus, J., Pensala, T., Kokkonen, K. & Jansman, A. Laterally coupled solidly mounted BAW resonators at 1.9 GHz. In *Ultrasonics Symposium (IUS), 2009 IEEE International*, 847–850 (2009).

[148] Pensala, T., Meltaus, J., Kokkonen, K. & Ylilammi, M. 2-D modeling of laterally acoustically coupled thin film bulk acoustic wave resonator filters. *Ultrasonics, Ferroelectrics and Frequency Control, IEEE Transactions on* **57**, 2537–2549 (2010).

BUSINESS +
ECONOMY

ART +
DESIGN +
ARCHITECTURE

SCIENCE +
TECHNOLOGY

CROSSOVER

DOCTORAL
DISSERTATIONS